doi:10.1038/nature10631

Contents

- Section A details our use of the *Kepler* data and provides important information deduced from the pulsation spectrum of KIC 05807616:
  - Section A.1 describes the extraction of the pulsation frequencies following a standard procedure, similar to the analysis of the star KPD 0629-0016 observed with CoRoT[31] or the star KIC 02697388 observed with Kepler[32] .
  - Section A.2 provides details on the detection of the low-frequency modulations attributed to orbiting bodies.
  - Section A.3 shows evidence for the presence of rotational splitting in the pulsation spectrum of KIC 05807616. A mean rotation period of approximately 39.23 days is estimated. Rotational splittings can provide extremely valuable information on the rotational status of stars[33] .
  - Section A.4 shows that constraints on the inclination angle of the system can be obtained from visibility arguments based on the observed amplitudes of components of well identified mode triplets. Mode visibilities can be computed accurately for sdB stars following Randall et al.[34] . Inclination angles lower than about 20° appear to be inconsistent with the observed triplet amplitudes. An inclination of approximately 65° is suggested.
- Section B shows, from pixel level light curve analysis, that the detected low-frequency signal comes from KIC 05807616 and not from a contaminating nearby star.
- Section C provides a discussion on various plausible origins for the low-frequency signal, but all alternative interpretations are ruled out for being either unlikely or inconsistent.
- Section D provides the calculations for evaluating the properties of the planet candidates from the measured signal. A complete exploration of the parameter space is presented. It shows with no ambiguity that in all situations except for very low inclination angles, objects of planetary size are expected. Low inclinations are however inconsistent with the observed properties of the pulsations (as detailed in section A.4) and can reasonably be ruled out. The analysis shows that in most cases, except when we assume that heat is evenly redistributed on the surface of the planet candidates (which seems unlikely for this system), nearly earth size bodies are predicted. At the opposite extreme, efficient heat distribution would imply Neptune/Jupiter size planets.
- Section E provides a discussion and hints for tentatively interpreting the F2 complex structure.

Supplementary Information, Section A: Frequencies detected in KIC 05807616 with Kepler

KIC 05807616's variability was first established during the *Kepler* exploration phase covered by quarters Q0 to Q4. During this phase, potentially interesting stars were alternately selected for observation in order to assess their potential for asteroseismology and decide if further monitoring with *Kepler* is relevant. Data for KIC 05807616 were obtained during the Q2.3 sub-run ($\sim$ 27 days of short cadence data sampled at 58.8 seconds) and the Q2 run (89 days of long cadence data sampled at 30 minutes)[11]. This star was not observed during quarters Q0, Q1, Q3, and Q4. Thus far, only the short cadence Q2.3 data have been used for a detailed asteroseismic study of KIC 05807616[15]. Q2 alone was not suitable for this purpose due to undersampling, as most of the oscillation modes have frequencies beyond the Nyquist limit for the long cadence data.

The short cadence *Kepler* monitoring of KIC 05807616 resumed in quarter Q5, nearly 6 months after Q2. From this time, it has been proceeding with no interruption other than those due to technical reasons. The detection of the low frequency modulations of interest and their interpretation first came after the Q5 data were released (in October 2010). The Q6 data (released in February 2011) provided insurance that these low signal-to-noise detections were indeed real. The 6 month monitoring offered by combining Q5+Q6 is the minimal contiguous data set that proves beyond any doubt (i.e., with a high enough signal-to-noise) that these frequencies exist. The Q5+Q6 data also resolve the fine structure in the pulsation spectrum that can be interpreted as rotational splitting and which is proving useful in the context of this study (see Section A.3 and A.4). Therefore, a significant part of the analysis presented below concentrates on the Q5+Q6 data only, unless their is some relevant benefit in including additional runs. By the time of this writing, Q7 has also been released (in May 2011), as well as Q8 (in August 2011).

A.1. Frequencies associated with pulsations

The analysis of the pulsations of KIC 05807616 (KPD 1943+4058) is based on the combined Q5 and Q6 *Kepler* runs which provide a sufficient basis for the purposes of this paper. In the spirit of having a homogeneous and contiguous short cadence light curve, we also avoided using Q2 in this context. We have analyzed in detail these data (corrected for flux contamination) following standard procedures based on prewhitening and nonlinear least-squares fitting techniques, similar to the analysis of the star KPD 0629-0016 observed with CoRoT[31] or the star KIC 02697388 observed with *Kepler*[32]. In the present case, this leads to the detection of 256 peaks emerging above the usual 4σ detection threshold and having frequencies higher than 60 μHz. Table A.3 provides the derived parameters for these peaks and Fig. A.1 illustrates the Lomb-Scargle periodograms in the most relevant region where the strongest pulsations occur. It is remarkable that among the frequencies detected, several emerge in the p-mode frequency range for a star like KIC 05807616 (above 3000 μHz; not shown in Fig. A.1 but see Table A.3). With the combined Q5 and Q6 data, this star shows evidence that it is also a hybrid pulsator with marginal – but clear – acoustic mode excitation. This would be quite compatible with the location of KIC 05807616 in the $\log g - T_{\rm eff}$ plane[15,32].

Many of these peaks form complexes of frequencies seemingly unresolved despite the very high frequency resolution already achieved with 6 months of monitoring (the formal resolution is 0.062 μHz). Most likely, this "hyperfine structure" should not be interpreted as real frequencies but must instead be related to varying amplitudes (and/or phases) of the excited pulsation modes over the period of observation. This interpretation is further supported by the fact that adding more data (Q2, Q7, and Q8, thus reaching a frequency resolution of 0.018 μHz) does not help in resolving these structures. Many other sdB stars observed with *Kepler* (with few exceptions) show this kind of behavior. Nevertheless, the presence of rotationally induced fine structure manifest through the presence of multiplets has also to be considered. In Sections A.3 and A.4, we investigate for signatures of rotation, as it may provide useful indications on the inclination angle of the system.

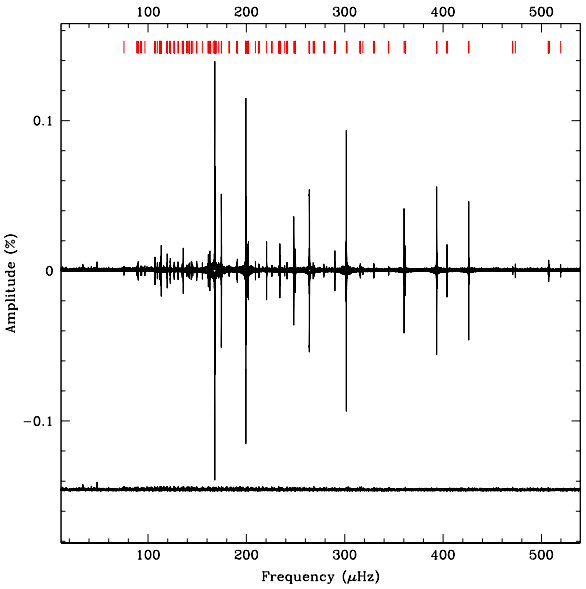

Figure A.1. Lomb-Scargle periodogram of the combined Q5 and Q6 data gathered on KIC 05807616 (curve shown at the top). The reconstruction of the modulations based on 256 frequencies associated with pulsations and known instrumental artifacts extracted from this light curve (see Table A.3) is plotted upside down. The curve at the bottom is the Lomb-Scargle periodogram of the residual light curve after subtraction of the 256 frequencies.

A.2. Weak modulations in the low frequency range

Figure A.2 shows close-up views of the amplitude spectra in the $31-51$ μHz range for the Q2 (long cadence), Q5+Q6, and Q6+Q7 data analyzed separately, as well as for the combined Q2+Q5-Q8 run. Two extremely low amplitude structures are clearly present in this frequency range. There are visible in all data subsets presented in Fig. A.2 and the detection of these peaks is secured beyond any doubt. We note that a third, much less certain, structure of even lower amplitude near 42.4 μHz is also apparent in the complete data set. However, its presence is at best suggestive in Q5+Q6 and Q7+Q8 and we will not consider it in detail in the following discussions. The parameters of these modulations are given in Table A.1. Figure 1 (main paper) also shows the Q2+Q5-Q8 light curve folded on F_1 and F_2 where these periodic modulations are clearly seen.

The time scales involved are 20 745 s (5.7625 hours) for the dominant modulation (F_1, detected at 9.3$\times$ the noise level

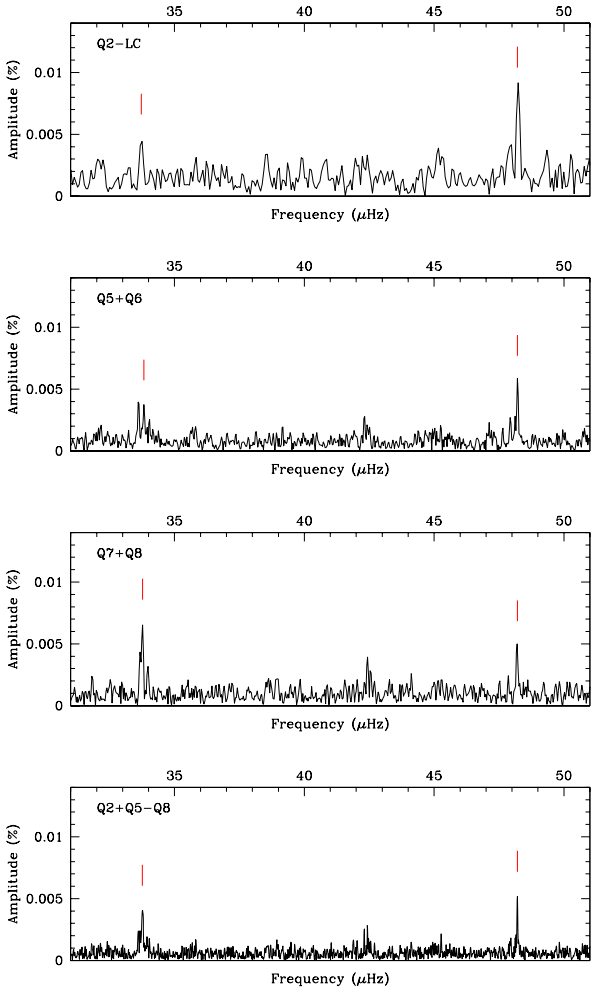

Figure A.2. Modulations in the low frequency range observed, from top to bottom, in the Q2 (long cadence), Q5+Q6, Q7+Q8, and in the combined Q2+Q5-Q8 runs.

with an amplitude of 52 ppm) and 29 625 s (8.2293 hours) for the other signal (F_2, detected at 8.4× the noise level with an amplitude of 47 ppm for the main component; but see Section E). The possible third structure has a timescale of 23 568 s (6.5467 hours; F_3, emerging at 5.2× the noise level in Q2+Q5-Q8 with an amplitude of 29 ppm). Throughout the 20 month time baseline of these data, the amplitude and phase of F_1 do not vary by more than 1σ between Q5+Q6 and Q7+Q8. It shows a slightly larger amplitude in the Q2 long cadence data, which remains within less than the 2σ error, however. These variations are therefore not significant and it is a clear indication that F_1 remains essentially stable in amplitude and phase (Table A.1). Another indication of this stability comes from the prewhitening of F_1 in the Q2+Q5-Q8 run (i.e., the subtraction of a pure sine wave to the entire light curve) that do not leave a detectable residual in Fourier space.

The picture appears more complicated for F_2 which is surrounded by a complex structure, possibly including components forming a nearly perfect triplet of frequency separation $\Delta\nu \sim 0.20\ \mu$Hz (most visible in the Q5+Q6 and Q2+Q5-Q8 runs). This

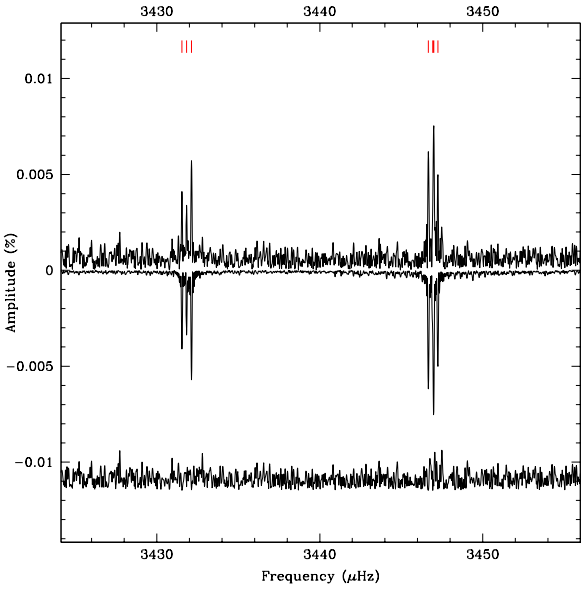

Figure A.3. Lomb-Scargle periodograms of the Q5+Q6 run showing two resolved triplets detected in the high frequency (p-mode) range.

complex structure is not resolved in the Q2 data (only 3 months), but is more apparent in the Q5+Q6, Q6+Q7 and Q2+Q5-Q8 runs (see Fig. A.2). In Section E, we provide arguments suggesting that this behavior may be caused by a frequency modulation producing a quasi-periodic signature in Fourier space.

A.3. Hints of rotation induced splittings

The signature of slow stellar rotation[33,35] is somewhat blurred by the presence of many close peaks originating from the non constant amplitudes or phases. We can however consider several mode complexes that seem to be relatively stable. Figure A.3 in particular shows two clear triplets in the $3430-3450\ \mu$Hz range (see also Table A.2 and A.3). The first triplet, $\{f_{142}, f_{198}, f_{079}\}$, shows frequency spacings of 0.29 and 0.30 μHz, respectively. The second triplet, $\{f_{062}, < f_{163}, f_{052} >, f_{085}\}$ has spacings of 0.31 and 0.28 μHz, respectively. Note that $< f_{163}, f_{052} >$ indicates the mean frequency value between these two very close components (attributed to the same mode). The two triplets therefore clearly show the same spacings of average value $\Delta\nu_p = 0.295\ \mu$Hz. Since these frequencies can be associated with p-modes with no ambiguity, the corresponding average rotation period for the star can be estimated as $P_{\rm rot} \sim 1/\Delta\nu_p = 39.2341$ days (at first order, assuming rigid rotation and neglecting the Ledoux coefficient which is normally very small for p-modes)[35].

If this rotational signature is present also for the g-modes, the asymptotic relation assuming solid rotation gives[35]

$$\Delta\nu_{g_\ell} \sim \left[1 - \frac{1}{\ell(\ell+1)}\right] \frac{1}{P_{\rm rot}} \qquad \text{(A.1)}$$

leading to expected splittings of $\Delta\nu_{g_1} \sim 0.148\ \mu$Hz, $\Delta\nu_{g_2} \sim 0.246\ \mu$Hz, and $\Delta\nu_{g_4} \sim 0.280\ \mu$Hz for g-modes of degree $\ell = 1$, 2, and 4, respectively. Figure A.4 and Table A.2 provide examples of relatively clear g-mode multiplets that conform to the above expectation in terms of frequency spacings between the m-components. This adds further strength to the interpretation

Table A.1. Orbital frequency candidates detected in the complete, Q2+Q5–Q8, data set and in several subsets: Q2 ($\sim$ 89 days in long cadence), Q5+Q6 ($\sim$ 186 days in short cadence), and Q6+Q7 ($\sim$ 172 days in short cadence). There is a gap of $\sim$ 185 days between the end of Q2 and beginning of Q5, while the Q5 to Q8 data are consecutive runs with only short interruptions. F_3 will require additional observations to be considered a secured detection. Note that in order to correctly check for the amplitude and phase stability of F_1 in the various data subsets, the frequency has been locked to the value measured with the full run (Q2+Q5-Q8). This cannot be done for F_2 which shows frequency variations. We also provide (in brackets), for comparison purposes with the experiments presented in Section E, the properties of the side components of F_2 forming an apparent triplet structure appearing most obviously in the Q5+Q6 sub-run.

Id.	Run	Frequency (μHz)	σ_f (μHz)	Period (s)	σ_P (s)	Amplitude (%)	σ_A (%)	Phase	$\sigma_{\rm Ph}$	S/N
F_1	**Q2+Q5–Q8**	**48.2040**	**0.0011**	**20745.17**	**0.47**	**0.0052**	**0.0006**	**0.59**	**0.05**	**9.3**
	Q2 (long cadence)	48.2040	0.0123	20746.17	5.31	0.0084	0.0014	0.61	0.07	5.8
	Q5+Q6	48.2040	0.0046	20746.17	1.99	0.0057	0.0008	0.64	0.02	7.4
	Q7+Q8	48.2040	0.0074	20746.17	3.21	0.0049	0.0010	0.65	0.03	5.0
F_2	**Q2+Q5–Q8**	**33.7547**	**0.0012**	**29625.52**	**1.05**	**0.0047**	**0.0006**	**0.40**	**0.15**	**8.4**
	Q2 (long cadence)	33.7238	0.0223	29652.64	19.65	0.0047	0.0014	0.72	0.24	3.2
		[33.6170]	[0.0055]	[29746.86]	[4.89]	[0.0044]	[0.0007]	[0.28]	[0.04]	[6.2]
	Q5+Q6	33.8269	0.0066	29562.27	5.76	0.0037	0.0007	0.40	0.05	5.2
		[34.0212]	[0.0096]	[29393.46]	[8.27]	[0.0025]	[0.0007]	[0.29]	[0.07]	[3.6]
	Q7+Q8	33.7670	0.0053	29614.70	4.66	0.0066	0.0010	0.97	0.04	7.0
F_3	Q2+Q5–Q8	42.4299	0.0020	23568.28	1.09	0.0029	0.0006	0.94	0.10	5.2

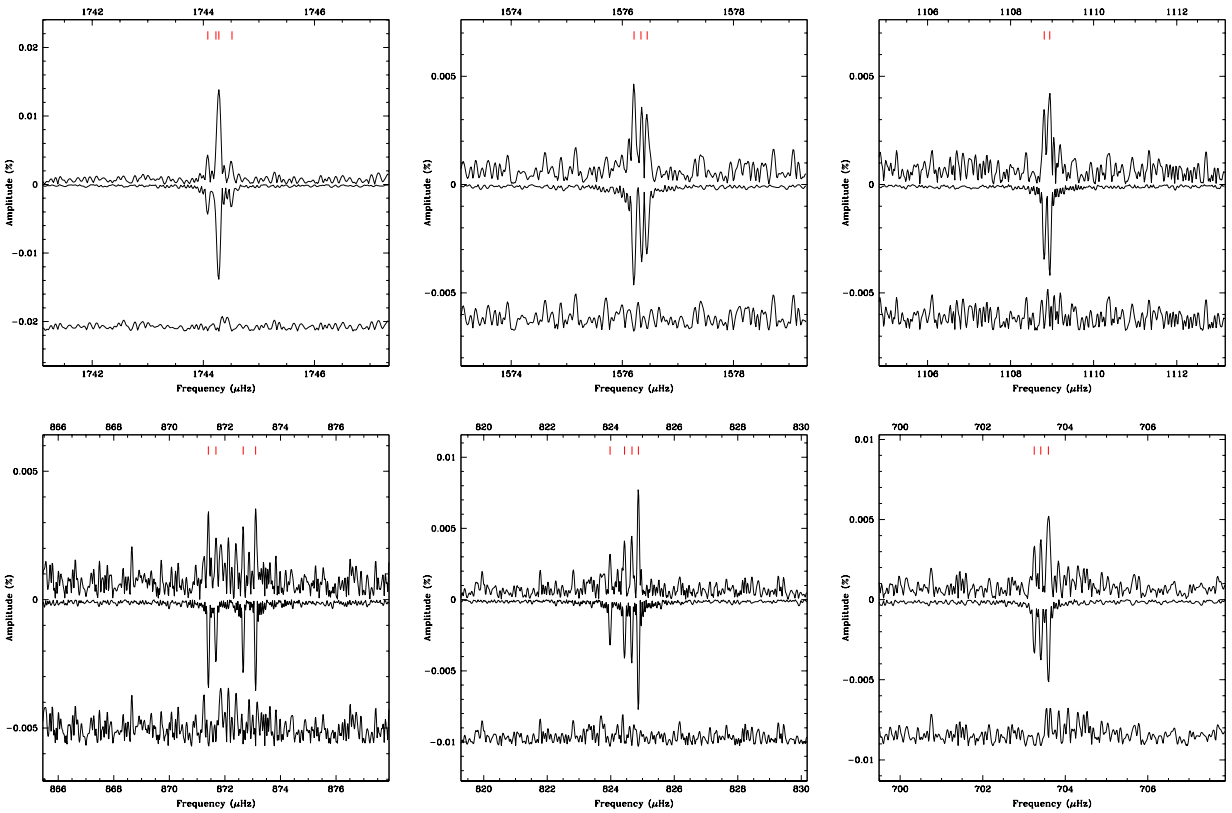

Figure A.4. Lomb-Scargle periodograms of the Q5+Q6 run showing a sample of clear multiplets detected in the low frequency (g-mode) range.

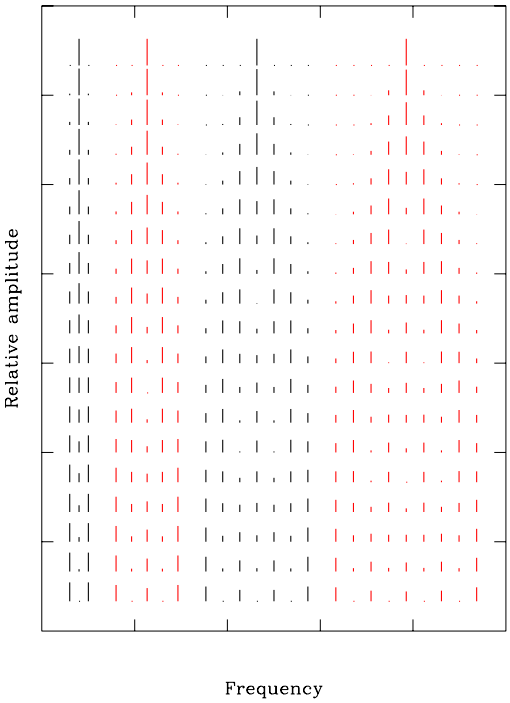

Figure A.5. Relative amplitude of $\ell = 1$, 2, 3, and 4 (from left to right) multiplet components split by rotation as a function of the inclination angle. From top to bottom, the configurations shown corresponds to inclinations angles from 0° (pole on) to 90° (equator on) by steps of 5°.

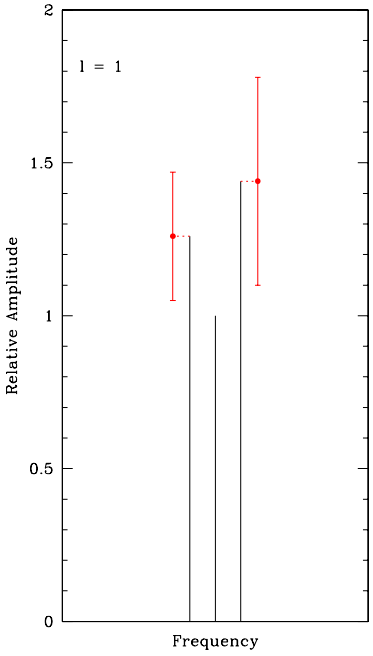

Figure A.6. Average relative amplitude built from 3 well defined $\ell = 1$ triplets (see Table A.2). The amplitude is normalized to 1 for the central component of each triplet (i.e., before the computation of the mean) and error bars indicate the standard deviation around this mean.

that we are indeed seeing the signature of slow rotation. Many other multiplets are likely present in Table A.3, but their identifications are not as clear due to interference with significant hyperfine structure around the peaks.

A.4. System inclination angle from mode visibility arguments

The identification of rotationally split multiplets can have a very interesting application. The geometric visibility of each *m*-component of a multiplet strongly depends on the inclination angle of the pulsation axis relative to the line of sight[36]. Mode visibilities can be computed accurately for sdB stars following Randall et al.[34] and this dependence is illustrated in Fig. A.5.

First, we assume as usual that the pulsation axis of the oscillations is naturally aligned with the rotation axis of the star. So far, this assumption has never been challenged observationally for sdB stars (oblique pulsators have a recognizable signature in Fourier space, like in RoAp stars[37]). In addition, the seismic analysis of the sdB star PG 1336-018 show that this alignment effectively exists in this case[38]. Second, the orbital plane of the planets is assumed coplanar with the equatorial plane of the star. The majority of the planetary systems are close to this configuration, although there are ongoing discussions on evidences of misaligned systems among the known hot Jupiters[39,40]. If we admit that the above configuration most likely prevails for KIC 05807616, then the inclination angle of the pulsation geometric configuration corresponds to the inclination angle, *i*, of the orbital system.

If the intrinsic amplitudes of the modes forming these multiplets were to be equal, the apparent amplitude ratios of the various components would reveal directly the value of this inclination angle. Clearly from observations, however, the intrinsic amplitudes are likely to differ from one mode to another, probably with modulations occurring on long timescales. While there exists no solid theoretical grounds to describe and predict quantitatively the intrinsic amplitudes of pulsations modes, we can note that, from the linear theory point of view, all the components of a given multiplet are expected, at least at first order, to have similar eigenfunctions. Their response to the mode driving mechanism is therefore not expected to strongly differ. In this context, it is reasonable to assume that all *m*-components of a given multiplet receive the same amount of excitation and, having similar inertia, develop to approximately the same intrinsic amplitude level. If other nonlinear mechanisms such as, e.g., energy transfers through resonant mode coupling may disturb this symmetry, one can think that, *on average*, the relative amplitude distribution in the multiplet components reflects mostly the geometrical factor, and hence the inclination of the system.

Looking at Table A.2, we emphasize that three triplets can naturally be associated with $\ell = 1$. For these modes, the detection of the three components (i.e., the complete triplet) permits the identification of the *m*-index of the modes. Several $\ell = 2$ complexes with 3 or 4 components are also well identified, but the *m*-values cannot be uniquely determined in these cases. Focusing hereafter on the three $\ell = 1$ triplets, we can construct from these a combined triplet of averaged relative amplitudes. For that purpose, we normalize the central component of each triplet to an arbitrary amplitude of 1 and rescale the amplitudes of the side components by the same factor, thus preserving the relative amplitude ratio between the components. The mean values (and

Table A.2. Sample of clearly identified multiplets that can be interpreted as rotational splittings. We provide a tentative ℓ-identification based on the observed spacings between the components. These values are derived from the Q5+Q6 data subset.

Id.	Frequency (μHz)	$\Delta\nu$ (μHz)	Amplitude (%)	Phase	Identification
f_{085}	3447.2455 ± 0.0039		0.0054 ± 0.0006	0.220 ± 0.032	
		0.278 ± 0.040			
$< f_{163}, f_{052} >$	3446.9678 ± 0.0400		0.0077 ± 0.0006	0.925 ± 0.011	$\ell = 2$
		0.308 ± 0.040			
f_{062}	3446.6596 ± 0.0031		0.0068 ± 0.0006	0.852 ± 0.025	
f_{079}	3432.1334 ± 0.0037		0.0057 ± 0.0006	0.857 ± 0.030	
		0.304 ± 0.007			
f_{198}	3431.8299 ± 0.0065		0.0032 ± 0.0006	0.129 ± 0.053	$\ell = 1$
		0.290 ± 0.008			
f_{142}	3431.5402 ± 0.0053		0.0039 ± 0.0006	0.254 ± 0.043	
f_{243}	1744.5154 ± 0.0082		0.0026 ± 0.0006	0.022 ± 0.064	
		0.235 ± 0.008			
f_{034} (f_{135})	1744.2802 ± 0.0016		0.0134 ± 0.0006	0.236 ± 0.007	$\ell = 2$
		0.200 ± 0.006			
f_{158}	1744.0805 ± 0.0058		0.0037 ± 0.0006	0.526 ± 0.046	
f_{226}	1576.4477 ± 0.0073		0.0029 ± 0.0006	0.979 ± 0.060	
		0.112 ± 0.010			
f_{222}	1576.3354 ± 0.0071		0.0030 ± 0.0006	0.519 ± 0.061	$\ell = 1$
		0.125 ± 0.009			
f_{112}	1576.2106 ± 0.0058		0.0046 ± 0.0006	0.611 ± 0.039	
f_{125}	1108.9424 ± 0.0051		0.0042 ± 0.0006	0.694 ± 0.041	
		0.132 ± 0.008			$\ell = 1$
f_{183}	1108.8106 ± 0.0063		0.0034 ± 0.0006	0.515 ± 0.051	
f_{181}	873.1052 ± 0.0063		0.0034 ± 0.0006	0.866 ± 0.049	
		0.448 ± 0.010			$\ell = 2$
f_{239}	872.6570 ± 0.0080		0.0027 ± 0.0006	0.994 ± 0.063	
f_{250}	871.6789 ± 0.0083		0.0026 ± 0.0006	0.760 ± 0.065	
		0.274 ± 0.010			$\ell = 4$
f_{161}	871.4045 ± 0.0059		0.0037 ± 0.0006	0.624 ± 0.046	
f_{055}	824.8685 ± 0.0029		0.0075 ± 0.0006	0.909 ± 0.023	
		0.202 ± 0.006			
f_{144}	824.6665 ± 0.0056		0.0039 ± 0.0006	0.087 ± 0.045	
		0.231 ± 0.008			$\ell = 2$
f_{136}	824.4359 ± 0.0053		0.0041 ± 0.0006	0.695 ± 0.042	
		0.457 ± 0.008			
f_{231}	823.9791 ± 0.0059		0.0028 ± 0.0006	0.864 ± 0.061	
f_{081}	703.5915 ± 0.0039		0.0055 ± 0.0006	0.234 ± 0.031	
		0.185 ± 0.007			
f_{178}	703.4065 ± 0.0062		0.0035 ± 0.0006	0.962 ± 0.051	$\ell = 1$
		0.158 ± 0.009			
f_{167}	703.2488 ± 0.0060		0.0036 ± 0.0006	0.105 ± 0.049	
f_{213}	226.0692 ± 0.0080		0.0031 ± 0.0007	0.250 ± 0.055	
		0.192 ± 0.011			$\ell = 2$?
f_{214}	225.8777 ± 0.0080		0.0031 ± 0.0007	0.322 ± 0.055	
f_{146}	182.5615 ± 0.0068		0.0039 ± 0.0008	0.966 ± 0.045	
		0.129 ± 0.010			$\ell = 1$
f_{160}	182.4330 ± 0.0071		0.0037 ± 0.0008	0.367 ± 0.047	

their standard deviations) of the rescaled amplitudes are then computed, leading to the average $\ell = 1$ triplet schematically illustrated in Fig. A.6. In this renormalized amplitude scale, the central component has, by construction, an amplitude $A_0 = 1$, and the side components have amplitudes $A_+ = 1.44 \pm 0.34$ and $A_- = 1.26 \pm 0.21$.

If we compare Fig. A.3, A.4, and A.6 with Fig. A.5, we find that the observed amplitude distribution within the rotationally split multiplets differs rather significantly from those expected for inclination angles $i \lesssim 20°$. This provides an interesting constraint on the system by suggesting that very low inclinations ($i \lesssim 20°$) are highly unlikely. If we further consider Fig. A.6 as the representative amplitude average for the $\ell = 1$ triplets, a direct comparison with the $\ell = 1$ modes shown in Fig. A.5 suggests that the inclination should be $\sim 65° \pm 10°$. This value should of course be considered as approximate keeping in mind, in particular, that only three complete triplets have been used to construct the amplitude averaged template shown in Fig. A.6.

Table A.3. Frequencies, f_n, detected above 4× the noise level and above 60 μHz based on the Q5+Q6 light curve (6 months).

Id.	Frequency (μHz)	σ_f (μHz)	Period (s)	σ_P (s)	Amplitude (%)	σ_A (%)	Phase	$\sigma_{\rm Ph}$	S/N
f_{206}	75.6448	0.0080	13219.674	1.394	0.0032	0.0007	0.728	0.053	4.3
f_{209}	88.4867	0.0081	11301.134	1.030	0.0031	0.0007	0.305	0.054	4.3
f_{220}	89.7206	0.0083	11145.710	1.036	0.0030	0.0007	0.402	0.056	4.1
f_{143}	89.9011	0.0065	11123.339	0.808	0.0039	0.0007	0.607	0.022	5.3
f_{073}	89.9694	0.0044	11114.891	0.547	0.0058	0.0007	0.652	0.015	7.8
f_{199}	92.4111	0.0079	10821.208	0.924	0.0032	0.0007	0.473	0.052	4.4
f_{202}	93.5459	0.0080	10689.943	0.913	0.0032	0.0007	0.393	0.053	4.3
f_{208}	96.8311	0.0081	10327.256	0.865	0.0031	0.0007	0.981	0.053	4.2
f_{046}	106.9312	0.0029	9351.812	0.252	0.0091	0.0008	0.420	0.019	11.9
f_{043}	107.0743	0.0028	9339.307	0.248	0.0092	0.0008	0.037	0.019	12.1
f_{203}	107.2851	0.0082	9320.963	0.715	0.0032	0.0008	0.804	0.055	4.2
f_{100}	109.4455	0.0052	9136.964	0.436	0.0050	0.0008	0.192	0.034	6.6
f_{108}	111.7006	0.0055	8952.507	0.443	0.0047	0.0008	0.374	0.036	6.2
f_{088}	111.8523	0.0049	8940.360	0.394	0.0053	0.0008	0.976	0.016	7.0
f_{149}	111.9247	0.0068	8934.582	0.540	0.0038	0.0008	0.727	0.022	5.1
f_{109}	112.0773	0.0056	8922.416	0.442	0.0047	0.0008	0.171	0.037	6.2
f_{118}	112.2582	0.0059	8908.035	0.471	0.0044	0.0008	0.676	0.020	5.8
f_{169}	112.3512	0.0073	8900.664	0.577	0.0036	0.0008	0.691	0.024	4.7
f_{165}	112.7462	0.0072	8869.480	0.568	0.0036	0.0008	0.950	0.047	4.8
f_{129}	113.2938	0.0063	8826.609	0.487	0.0042	0.0008	0.548	0.020	5.5
f_{021}	113.3621	0.0015	8821.287	0.115	0.0175	0.0008	0.003	0.005	23.2
f_{053}	113.4197	0.0034	8816.814	0.264	0.0077	0.0008	0.372	0.011	10.1
f_{040}	113.5626	0.0027	8805.716	0.207	0.0097	0.0008	0.194	0.018	12.9
f_{078}	119.3725	0.0046	8377.140	0.322	0.0057	0.0008	0.302	0.030	7.5
f_{037}	119.5451	0.0022	8365.045	0.153	0.0119	0.0008	0.695	0.007	15.7
f_{110}	119.6006	0.0056	8361.165	0.389	0.0047	0.0008	0.560	0.018	6.2
f_{175}	119.7576	0.0074	8350.198	0.516	0.0035	0.0008	0.815	0.048	4.6
f_{180}	122.3797	0.0076	8171.289	0.507	0.0034	0.0008	0.702	0.050	4.5
f_{048}	122.6261	0.0029	8154.871	0.192	0.0091	0.0008	0.824	0.009	11.9
f_{066}	122.6840	0.0040	8151.021	0.267	0.0065	0.0008	0.022	0.013	8.6
f_{162}	122.7690	0.0071	8145.380	0.471	0.0037	0.0008	0.218	0.024	4.8
f_{101}	126.4964	0.0053	7905.365	0.334	0.0049	0.0008	0.659	0.035	6.4
f_{182}	126.6838	0.0077	7893.669	0.477	0.0034	0.0008	0.299	0.050	4.5
f_{159}	126.8370	0.0071	7884.137	0.439	0.0037	0.0008	0.298	0.024	4.9
f_{168}	126.8868	0.0073	7881.038	0.454	0.0036	0.0008	0.201	0.024	4.7
f_{076}	130.5418	0.0046	7660.380	0.271	0.0057	0.0008	0.797	0.030	7.4
f_{172}	130.8423	0.0074	7642.790	0.431	0.0035	0.0008	0.323	0.048	4.7
f_{106}	134.6592	0.0055	7426.156	0.304	0.0047	0.0008	0.797	0.036	6.2
f_{196}	135.3763	0.0080	7386.816	0.434	0.0033	0.0008	0.231	0.052	4.3
f_{060}	135.6855	0.0038	7369.985	0.206	0.0069	0.0008	0.185	0.013	9.1
f_{033}	135.7344	0.0019	7367.327	0.102	0.0138	0.0008	0.962	0.006	18.2
f_{058}	135.7930	0.0037	7364.150	0.199	0.0071	0.0008	0.563	0.012	9.4
f_{122}	135.9742	0.0062	7354.338	0.333	0.0042	0.0008	0.634	0.041	5.6
f_{148}	139.5183	0.0068	7167.520	0.348	0.0039	0.0008	0.676	0.044	5.1
f_{212}	139.9032	0.0084	7147.800	0.428	0.0031	0.0008	0.920	0.054	4.1
f_{103}	141.8502	0.0054	7049.689	0.269	0.0048	0.0008	0.930	0.036	6.3
f_{114}	141.9475	0.0057	7044.858	0.283	0.0046	0.0008	0.095	0.019	6.0
f_{091}	142.0372	0.0050	7040.408	0.247	0.0052	0.0008	0.996	0.017	6.9
f_{187}	142.1539	0.0077	7034.631	0.383	0.0034	0.0008	0.004	0.026	4.4
f_{119}	142.2074	0.0060	7031.983	0.297	0.0043	0.0008	0.264	0.020	5.7
f_{069}	144.0234	0.0042	6943.318	0.201	0.0063	0.0008	0.816	0.028	8.2
f_{151}	144.2236	0.0069	6933.679	0.330	0.0038	0.0008	0.082	0.049	5.0
f_{071}	144.3298	0.0044	6928.578	0.209	0.0060	0.0008	0.207	0.031	7.9
f_{127}	144.5139	0.0063	6919.748	0.300	0.0042	0.0008	0.662	0.041	5.5
f_{200}	145.6003	0.0081	6868.116	0.382	0.0032	0.0008	0.724	0.052	4.2
f_{171}	149.5202	0.0073	6688.061	0.327	0.0035	0.0008	0.458	0.049	4.7
f_{065}	149.6295	0.0039	6683.176	0.176	0.0066	0.0008	0.952	0.026	8.7

Table A.3. continued.

Id.	Frequency (μHz)	σ_f (μHz)	Period (s)	σ_P (s)	Amplitude (%)	σ_A (%)	Phase	$\sigma_{\rm Ph}$	S/N
f_{086}	155.3069	0.0048	6438.862	0.201	0.0054	0.0008	0.998	0.031	7.1
f_{093}	161.1882	0.0051	6203.927	0.194	0.0052	0.0008	0.936	0.033	6.8
f_{042}	161.3460	0.0028	6197.859	0.108	0.0093	0.0008	0.927	0.018	12.2
f_{132}	161.6159	0.0064	6187.511	0.244	0.0041	0.0008	0.183	0.042	5.4
f_{193}	162.8780	0.0080	6139.565	0.301	0.0033	0.0008	0.429	0.052	4.3
f_{027}	163.0190	0.0017	6134.254	0.064	0.0155	0.0008	0.622	0.006	20.3
f_{115}	163.1037	0.0058	6131.068	0.216	0.0046	0.0008	0.136	0.019	6.0
f_{087}	163.2855	0.0049	6124.243	0.185	0.0053	0.0008	0.154	0.032	7.0
f_{194}	166.3649	0.0080	6010.883	0.290	0.0033	0.0008	0.009	0.051	4.3
f_{063}	167.5458	0.0040	5968.517	0.141	0.0066	0.0008	0.127	0.013	8.7
f_{041}	167.6183	0.0028	5965.934	0.100	0.0094	0.0008	0.769	0.009	12.2
f_{013}	167.6754	0.0009	5963.903	0.033	0.0281	0.0008	0.734	0.003	36.6
f_{017}	167.7552	0.0013	5961.068	0.047	0.0200	0.0008	0.497	0.004	26.1
f_{001}	167.8359	0.0002	5958.203	0.007	0.1421	0.0008	0.218	0.001	185.1
f_{012}	167.8924	0.0008	5956.197	0.029	0.0318	0.0008	0.469	0.003	41.4
f_{025}	167.9783	0.0016	5953.151	0.055	0.0170	0.0008	0.632	0.005	22.1
f_{137}	168.0276	0.0066	5951.403	0.232	0.0040	0.0008	0.404	0.022	5.2
f_{004}	168.0867	0.0004	5949.310	0.013	0.0707	0.0008	0.600	0.001	92.2
f_{072}	168.2074	0.0045	5945.042	0.157	0.0059	0.0008	0.485	0.015	7.7
f_{117}	168.2920	0.0059	5942.054	0.208	0.0045	0.0008	0.138	0.019	5.8
f_{192}	169.4617	0.0080	5901.039	0.278	0.0033	0.0008	0.534	0.051	4.3
f_{177}	171.8123	0.0076	5820.307	0.257	0.0035	0.0008	0.744	0.048	4.5
f_{008}	174.6127	0.0005	5726.960	0.017	0.0508	0.0008	0.459	0.003	66.1
f_{050}	174.7171	0.0030	5723.539	0.099	0.0088	0.0008	0.990	0.020	11.4
f_{160}	182.4330	0.0071	5481.465	0.212	0.0037	0.0008	0.367	0.047	4.9
f_{146}	182.5615	0.0068	5477.606	0.203	0.0039	0.0008	0.966	0.045	5.1
f_{134}	190.3977	0.0063	5252.165	0.175	0.0041	0.0008	0.319	0.041	5.4
f_{080}	190.6964	0.0047	5243.938	0.129	0.0055	0.0008	0.765	0.015	7.3
f_{057}	190.7625	0.0035	5242.121	0.097	0.0073	0.0008	0.941	0.012	9.7
f_{174}	190.8411	0.0074	5239.962	0.202	0.0035	0.0008	0.541	0.024	4.7
f_{102}	199.1823	0.0053	5020.527	0.133	0.0049	0.0007	0.799	0.018	6.5
f_{036}	199.2625	0.0021	5018.506	0.053	0.0122	0.0008	0.365	0.007	16.2
f_{068}	199.3226	0.0041	5016.993	0.103	0.0063	0.0007	0.587	0.014	8.4
f_{049}	199.3877	0.0028	5015.355	0.072	0.0091	0.0007	0.350	0.010	12.1
f_{014}	199.4349	0.0009	5014.168	0.024	0.0274	0.0007	0.749	0.003	36.6
f_{002}	199.5135	0.0002	5012.191	0.006	0.1112	0.0007	0.715	0.001	148.4
f_{029}	199.5840	0.0018	5010.423	0.045	0.0143	0.0007	0.424	0.006	19.1
f_{139}	199.6285	0.0064	5009.305	0.161	0.0040	0.0007	0.697	0.023	5.4
f_{089}	201.4199	0.0049	4964.752	0.121	0.0052	0.0007	0.733	0.036	7.0
f_{131}	201.5208	0.0062	4962.266	0.153	0.0041	0.0007	0.857	0.048	5.5
f_{015}	201.6606	0.0012	4958.826	0.030	0.0214	0.0007	0.118	0.009	28.6
f_{016}	201.7564	0.0012	4956.472	0.030	0.0210	0.0007	0.434	0.004	27.9
f_{090}	201.8210	0.0049	4954.886	0.121	0.0052	0.0007	0.597	0.017	7.0
f_{097}	201.9051	0.0051	4952.823	0.125	0.0051	0.0007	0.474	0.017	6.8
f_{038}	201.9811	0.0025	4950.959	0.062	0.0103	0.0007	0.081	0.009	13.7
f_{020}	202.0995	0.0014	4948.058	0.034	0.0188	0.0008	0.462	0.005	25.1
f_{153}	202.1496	0.0068	4946.831	0.166	0.0038	0.0008	0.796	0.023	5.1
f_{070}	209.1975	0.0041	4780.171	0.095	0.0062	0.0007	0.155	0.027	8.3
f_{164}	212.6202	0.0069	4703.221	0.153	0.0036	0.0007	0.292	0.047	5.0
f_{107}	212.7151	0.0054	4701.124	0.118	0.0047	0.0007	0.818	0.019	6.4
f_{123}	212.7953	0.0060	4699.352	0.132	0.0042	0.0007	0.132	0.021	5.7
f_{018}	220.6189	0.0013	4532.703	0.026	0.0196	0.0007	0.513	0.009	26.7
f_{214}	225.8777	0.0080	4427.175	0.158	0.0031	0.0007	0.322	0.055	4.3
f_{213}	226.0692	0.0080	4423.425	0.157	0.0031	0.0007	0.250	0.055	4.3
f_{211}	232.7409	0.0079	4296.623	0.147	0.0031	0.0007	0.095	0.055	4.3
f_{197}	232.9742	0.0076	4292.322	0.140	0.0033	0.0007	0.893	0.052	4.5
f_{140}	233.8258	0.0062	4276.689	0.114	0.0040	0.0007	0.787	0.045	5.5
f_{084}	233.9401	0.0046	4274.598	0.083	0.0054	0.0007	0.041	0.033	7.5

Table A.3. continued.

Id.	Frequency (μHz)	σ_f (μHz)	Period (s)	σ_P (s)	Amplitude (%)	σ_A (%)	Phase	$\sigma_{\rm Ph}$	S/N
f_{039}	234.0824	0.0025	4271.999	0.046	0.0098	0.0007	0.621	0.009	13.6
f_{019}	234.1461	0.0013	4270.838	0.024	0.0188	0.0007	0.244	0.005	26.1
f_{095}	234.2067	0.0049	4269.733	0.089	0.0051	0.0007	0.670	0.017	7.1
f_{045}	234.2646	0.0027	4268.677	0.050	0.0091	0.0007	0.956	0.010	12.6
f_{113}	234.3893	0.0054	4266.407	0.098	0.0046	0.0007	0.677	0.039	6.4
f_{155}	239.0130	0.0065	4183.872	0.114	0.0038	0.0007	0.910	0.045	5.3
f_{150}	241.1608	0.0064	4146.611	0.110	0.0038	0.0007	0.903	0.022	5.4
f_{082}	241.2171	0.0045	4145.643	0.076	0.0055	0.0007	0.154	0.016	7.7
f_{152}	241.3839	0.0064	4142.778	0.110	0.0038	0.0007	0.124	0.047	5.3
f_{130}	241.5383	0.0059	4140.130	0.101	0.0041	0.0007	0.510	0.044	5.8
f_{075}	241.6346	0.0043	4138.481	0.073	0.0057	0.0007	0.583	0.031	8.1
f_{011}	248.3190	0.0007	4027.078	0.011	0.0369	0.0007	0.388	0.005	52.1
f_{077}	249.4774	0.0043	4008.380	0.069	0.0057	0.0007	0.151	0.015	8.0
f_{104}	249.5606	0.0051	4007.043	0.082	0.0048	0.0007	0.697	0.018	6.7
f_{030}	249.6199	0.0017	4006.091	0.027	0.0142	0.0007	0.904	0.006	20.0
f_{061}	249.6769	0.0035	4005.177	0.057	0.0068	0.0007	0.085	0.013	9.7
f_{096}	249.7350	0.0048	4004.245	0.077	0.0051	0.0007	0.389	0.017	7.2
f_{031}	249.8666	0.0017	4002.135	0.028	0.0140	0.0007	0.135	0.013	19.8
f_{092}	264.0237	0.0045	3787.539	0.065	0.0052	0.0007	0.710	0.017	7.6
f_{007}	264.0748	0.0004	3786.805	0.006	0.0537	0.0007	0.874	0.002	77.8
f_{005}	264.1295	0.0004	3786.021	0.006	0.0577	0.0007	0.142	0.002	83.6
f_{056}	264.1764	0.0032	3785.350	0.046	0.0074	0.0007	0.380	0.013	10.8
f_{083}	267.9364	0.0043	3732.229	0.060	0.0055	0.0007	0.091	0.031	8.0
f_{189}	268.8341	0.0071	3719.766	0.098	0.0033	0.0007	0.821	0.051	4.8
f_{141}	269.0908	0.0060	3716.218	0.083	0.0039	0.0007	0.217	0.043	5.7
f_{124}	278.8880	0.0055	3585.668	0.071	0.0042	0.0007	0.872	0.040	6.2
f_{230}	279.1875	0.0083	3581.822	0.107	0.0028	0.0007	0.331	0.060	4.1
f_{133}	289.7878	0.0056	3450.801	0.067	0.0041	0.0007	0.398	0.021	6.1
f_{210}	289.8550	0.0073	3450.001	0.087	0.0031	0.0007	0.629	0.027	4.7
f_{035}	290.1219	0.0019	3446.827	0.022	0.0123	0.0007	0.602	0.007	18.4
f_{145}	290.2048	0.0059	3445.843	0.070	0.0039	0.0007	0.485	0.022	5.8
f_{170}	290.3220	0.0064	3444.451	0.076	0.0036	0.0007	0.593	0.049	5.3
f_{003}	301.6656	0.0002	3314.929	0.003	0.0955	0.0007	0.608	0.002	145.2
f_{173}	302.3627	0.0064	3307.286	0.070	0.0035	0.0007	0.254	0.047	5.4
f_{216}	315.5807	0.0072	3168.762	0.072	0.0031	0.0007	0.185	0.055	4.8
f_{099}	315.7905	0.0044	3166.657	0.044	0.0050	0.0007	0.205	0.018	7.7
f_{157}	315.8385	0.0060	3166.175	0.060	0.0037	0.0007	0.474	0.024	5.7
f_{179}	316.1603	0.0065	3162.952	0.065	0.0034	0.0006	0.389	0.049	5.3
f_{242}	318.6196	0.0084	3138.539	0.082	0.0027	0.0006	0.322	0.063	4.1
f_{074}	329.6745	0.0039	3033.295	0.035	0.0057	0.0006	0.242	0.033	8.9
f_{094}	329.7726	0.0043	3032.393	0.040	0.0051	0.0006	0.431	0.037	8.0
f_{126}	330.0955	0.0053	3029.427	0.048	0.0042	0.0006	0.598	0.040	6.5
f_{241}	344.4841	0.0082	2902.892	0.069	0.0027	0.0006	0.334	0.064	4.2
f_{247}	344.7887	0.0084	2900.327	0.070	0.0026	0.0006	0.000	0.065	4.1
f_{010}	360.4300	0.0005	2774.464	0.004	0.0425	0.0006	0.178	0.004	67.4
f_{024}	361.6834	0.0013	2764.849	0.010	0.0171	0.0006	0.568	0.005	27.1
f_{059}	361.7446	0.0031	2764.381	0.024	0.0069	0.0006	0.841	0.012	11.0
f_{156}	361.8166	0.0058	2763.831	0.044	0.0038	0.0006	0.447	0.023	6.0
f_{120}	393.5186	0.0051	2541.176	0.033	0.0043	0.0006	0.779	0.021	6.8
f_{023}	393.5696	0.0013	2540.847	0.008	0.0172	0.0006	0.849	0.005	27.3
f_{006}	393.6183	0.0004	2540.533	0.002	0.0573	0.0006	0.729	0.002	90.7
f_{205}	403.9420	0.0068	2475.603	0.042	0.0032	0.0006	0.385	0.030	5.0
f_{022}	403.9841	0.0012	2475.345	0.008	0.0173	0.0006	0.254	0.005	27.5
f_{201}	404.0426	0.0068	2474.986	0.041	0.0032	0.0006	0.949	0.027	5.1
f_{128}	426.0790	0.0052	2346.983	0.029	0.0042	0.0006	0.864	0.020	6.6
f_{009}	426.1331	0.0005	2346.685	0.003	0.0463	0.0006	0.240	0.002	73.6
f_{249}	470.7497	0.0083	2124.271	0.037	0.0026	0.0006	0.632	0.065	4.2
f_{244}	470.9925	0.0081	2123.176	0.037	0.0026	0.0006	0.048	0.064	4.2

Table A.3. continued.

Id.	Frequency (μHz)	σ_f (μHz)	Period (s)	σ_P (s)	Amplitude (%)	σ_A (%)	Phase	$\sigma_{\rm Ph}$	S/N
f_{116}	473.5820	0.0047	2111.567	0.021	0.0045	0.0006	0.991	0.037	7.3
f_{251}	506.9636	0.0084	1972.528	0.033	0.0026	0.0006	0.882	0.066	4.1
f_{224}	507.4432	0.0073	1970.664	0.029	0.0029	0.0006	0.835	0.057	4.7
f_{064}	507.5871	0.0033	1970.105	0.013	0.0066	0.0006	0.528	0.013	10.5
f_{235}	507.6593	0.0080	1969.825	0.031	0.0027	0.0006	0.556	0.032	4.3
f_{121}	519.7064	0.0051	1924.163	0.019	0.0043	0.0006	0.204	0.039	6.8
f_{188}	625.8779	0.0064	1597.756	0.016	0.0034	0.0006	0.861	0.050	5.4
f_{184}	654.6297	0.0064	1527.581	0.015	0.0034	0.0006	0.750	0.051	5.4
f_{229}	654.7753	0.0075	1527.241	0.018	0.0029	0.0006	0.232	0.060	4.6
f_{190}	669.6476	0.0065	1493.323	0.014	0.0033	0.0006	0.671	0.051	5.3
f_{176}	670.2628	0.0061	1491.952	0.014	0.0035	0.0006	0.616	0.048	5.6
f_{221}	699.2945	0.0071	1430.013	0.015	0.0030	0.0006	0.858	0.056	4.8
f_{167}	703.2488	0.0060	1421.972	0.012	0.0036	0.0006	0.105	0.049	5.7
f_{178}	703.4065	0.0062	1421.653	0.013	0.0035	0.0006	0.962	0.051	5.5
f_{081}	703.5915	0.0039	1421.279	0.008	0.0055	0.0006	0.234	0.031	8.8
f_{204}	758.2632	0.0066	1318.803	0.012	0.0032	0.0006	0.433	0.053	5.2
f_{231}	823.9791	0.0078	1213.623	0.011	0.0028	0.0006	0.864	0.061	4.4
f_{136}	824.4359	0.0053	1212.951	0.008	0.0041	0.0006	0.695	0.042	6.5
f_{144}	824.6665	0.0056	1212.611	0.008	0.0039	0.0006	0.087	0.045	6.2
f_{055}	824.8685	0.0029	1212.314	0.004	0.0075	0.0006	0.909	0.023	11.8
f_{228}	858.9581	0.0076	1164.201	0.010	0.0029	0.0006	0.644	0.059	4.5
f_{161}	871.4045	0.0059	1147.573	0.008	0.0037	0.0006	0.624	0.046	5.8
f_{250}	871.6789	0.0083	1147.211	0.011	0.0026	0.0006	0.760	0.065	4.1
f_{239}	872.6570	0.0080	1145.926	0.011	0.0027	0.0006	0.994	0.063	4.3
f_{181}	873.1052	0.0063	1145.337	0.008	0.0034	0.0006	0.866	0.049	5.4
f_{183}	1108.8106	0.0063	901.867	0.005	0.0034	0.0006	0.515	0.051	5.5
f_{125}	1108.9424	0.0051	901.760	0.004	0.0042	0.0006	0.694	0.041	6.8
f_{207}	1174.6188	0.0068	851.340	0.005	0.0032	0.0006	0.795	0.053	5.1
f_{215}	1449.4730	0.0069	689.906	0.003	0.0031	0.0006	0.438	0.054	5.0
f_{240}	1494.5229	0.0080	669.110	0.004	0.0027	0.0006	0.501	0.063	4.3
f_{232}	1527.6849	0.0077	654.585	0.003	0.0028	0.0006	0.376	0.061	4.4
f_{186}	1542.7341	0.0063	648.200	0.003	0.0034	0.0006	0.674	0.050	5.4
f_{112}	1576.2106	0.0046	634.433	0.002	0.0046	0.0006	0.611	0.039	7.5
f_{222}	1576.3354	0.0071	634.383	0.003	0.0030	0.0006	0.519	0.061	4.9
f_{226}	1576.4477	0.0073	634.338	0.003	0.0029	0.0006	0.979	0.060	4.7
f_{236}	1630.9230	0.0079	613.150	0.003	0.0027	0.0006	0.199	0.062	4.3
f_{225}	1648.3471	0.0073	606.668	0.003	0.0029	0.0006	0.708	0.057	4.7
f_{158}	1744.0805	0.0058	573.368	0.002	0.0037	0.0006	0.526	0.046	5.9
f_{135}	1744.2279	0.0053	573.320	0.002	0.0041	0.0006	0.499	0.021	6.5
f_{034}	1744.2802	0.0016	573.302	0.001	0.0134	0.0006	0.236	0.007	21.3
f_{243}	1744.5154	0.0082	573.225	0.003	0.0026	0.0006	0.022	0.064	4.2
f_{253}	1786.7102	0.0084	559.688	0.003	0.0025	0.0006	0.208	0.067	4.1
f_{185}	1834.9865	0.0062	544.963	0.002	0.0034	0.0006	0.480	0.050	5.5
f_{142}	3431.5402	0.0053	291.414	0.000	0.0039	0.0006	0.254	0.043	6.5
f_{198}	3431.8299	0.0065	291.390	0.001	0.0032	0.0006	0.129	0.053	5.3
f_{079}	3432.1334	0.0037	291.364	0.000	0.0057	0.0006	0.857	0.030	9.3
f_{062}	3446.6596	0.0031	290.136	0.000	0.0068	0.0006	0.852	0.025	11.0
f_{163}	3446.9397	0.0058	290.112	0.000	0.0037	0.0006	0.181	0.023	6.0
f_{052}	3446.9958	0.0027	290.108	0.000	0.0077	0.0006	0.925	0.011	12.6
f_{085}	3447.2455	0.0039	290.087	0.000	0.0054	0.0006	0.220	0.032	8.8
f_{255}	3970.4852	0.0084	251.858	0.001	0.0025	0.0006	0.620	0.067	4.1
f_{246}	4512.7282	0.0080	221.595	0.000	0.0026	0.0006	0.832	0.067	4.3
f_{217}	4512.8417	0.0068	221.590	0.000	0.0031	0.0006	0.702	0.057	5.1
f_{227}	4514.2984	0.0072	221.518	0.000	0.0029	0.0006	0.439	0.030	4.7
f_{166}	4514.3906	0.0058	221.514	0.000	0.0036	0.0006	0.620	0.025	5.9
f_{238}	4514.5094	0.0078	221.508	0.000	0.0027	0.0006	0.910	0.065	4.4
f_{233}	5516.7338	0.0078	181.267	0.000	0.0028	0.0006	0.679	0.061	4.4
f_{254}	5842.3897	0.0084	171.163	0.000	0.0025	0.0006	0.107	0.067	4.1

Table A.3. continued.

Id.	Frequency (μHz)	σ_f (μHz)	Period (s)	σ_P (s)	Amplitude (%)	σ_A (%)	Phase	$\sigma_{\rm Ph}$	S/N
f_{256}	8005.6126	0.0086	124.912	0.000	0.0025	0.0006	0.621	0.068	4.0
Instrumental artefacts									
$a_{245} : f_{\rm LC}$	566.4057	0.0082	1765.519	0.026	0.0026	0.0006	0.944	0.064	4.2
$a_{195} : 2f_{\rm LC}$	1132.8254	0.0065	882.749	0.005	0.0033	0.0006	0.920	0.051	5.3
$a_{237} : 3f_{\rm LC}$	1699.2179	0.0080	588.506	0.003	0.0027	0.0006	0.985	0.062	4.3
a_{234}	3398.3477	0.0077	294.261	0.001	0.0027	0.0006	0.175	0.031	4.5
$a_{191} : 6f_{\rm LC}$	3398.3997	0.0063	294.256	0.001	0.0033	0.0006	0.091	0.026	5.4
a_{248}	3964.7115	0.0080	252.225	0.001	0.0026	0.0006	0.398	0.032	4.3
$a_{067} : 7f_{\rm LC}$	3964.7790	0.0033	252.221	0.000	0.0064	0.0006	0.058	0.014	10.4
a_{138}	3964.8263	0.0052	252.218	0.000	0.0040	0.0006	0.945	0.022	6.6
a_{044}	4531.1411	0.0023	220.695	0.000	0.0092	0.0006	0.737	0.009	15.0
a_{026}	4531.2088	0.0013	220.692	0.000	0.0163	0.0006	0.325	0.005	26.6
a_{105}	4531.2615	0.0045	220.689	0.000	0.0047	0.0006	0.962	0.018	7.7
a_{032}	4531.3327	0.0015	220.686	0.000	0.0140	0.0006	0.180	0.006	22.8
$a_{028} : 8f_{\rm LC}$	4531.3917	0.0014	220.683	0.000	0.0153	0.0006	0.381	0.006	24.8
a_{051}	4531.4483	0.0025	220.680	0.000	0.0086	0.0006	0.579	0.010	14.0
a_{218}	4531.5242	0.0068	220.676	0.000	0.0031	0.0006	0.476	0.028	5.0
a_{111}	5097.5092	0.0046	196.174	0.000	0.0047	0.0006	0.011	0.019	7.5
$a_{047} : 9f_{\rm LC}$	5097.5893	0.0023	196.171	0.000	0.0091	0.0006	0.567	0.010	14.8
a_{054}	5097.6370	0.0028	196.169	0.000	0.0075	0.0006	0.496	0.012	12.1
a_{098}	5097.7578	0.0042	196.165	0.000	0.0051	0.0006	0.449	0.035	8.2
a_{219}	5663.9437	0.0067	176.555	0.000	0.0031	0.0006	0.718	0.028	5.1
$a_{147} : 10f_{\rm LC}$	5663.9948	0.0053	176.554	0.000	0.0039	0.0006	0.586	0.022	6.4
a_{252}	5664.2110	0.0080	176.547	0.000	0.0026	0.0006	0.200	0.066	4.3
$a_{223} : 11f_{\rm LC}$	6230.3659	0.0071	160.504	0.000	0.0030	0.0006	0.714	0.057	4.8
$a_{154} : 14f_{\rm LC}$	7929.5560	0.0055	126.110	0.000	0.0038	0.0006	0.786	0.044	6.2

Supplementary Information, Section B: Rejecting a false positive detection due to contamination with pixel level light curve analysis

The risk that a fainter background or foreground star could be at the origin of the low frequency modulations has to be considered. The frequency analysis of the light curve based on the raw and corrected fluxes (we used the corrected fluxes as the reference in this analysis) do not lead to significant amplitude differences. This suggests that light contamination from other nearby stars in the optimal aperture may be negligible and the risk is low. Nevertheless, this star is located in a relatively densely populated region with several sources close by that may possibly contribute to the light curve gathered by the instrument (see Fig. B.1). We show below that the origin of the detected signal is very likely KIC 05807616 (KPD 1943+4058) itself and not a contaminating star.

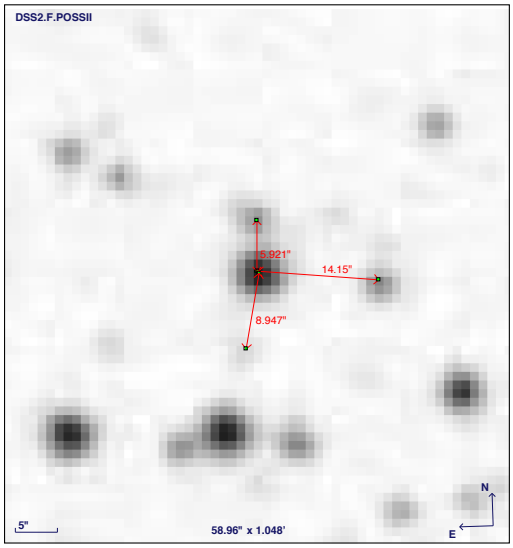

Figure B.1. The field centered on KIC 05807616 with angular distances from the closest neighbors (the software Aladin was used to produce this map).

In order to verify the localization of the detected signal and rule out an eventual false positive detection due to a contaminating nearby star, the pixel level photometry available from the *Kepler* data can be very useful. Figure B.1 shows the close neighborhood of KIC 05807616 as seen from the Digitized Sky Survey. A fainter star, approximately 6" North of KIC 05807616 can in particular be a significant source of contamination, considering that the angular resolution at the pixel level on the *Kepler* CCDs is 3.98". This star is probably the main object of concern, as no other known object within a 8" radius around KIC 05807616 is referenced in current catalogs or visible in sky images. Figure B.2 shows the approximate position of the mask used during the Q5 run and confirms that light from this nearby star can likely leak into some pixels that have been used to construct the optimal aperture photometric light curve (i.e., the red pixels in Fig. B.2).

As a first check, we constructed several 3-month duration light curves (from Q5) by adding pixels belonging to different quadrants around KIC 05807616. A "North-East light curve" was built with pixels $P_{2,3}$, $P_{2,2}$, $P_{3,2}$, $P_{3,1}$, and $P_{4,1}$ ($P_{x,y}$ corresponds to column x and row y); a "North-West light curve" from pixels $P_{4,1}$, $P_{5,1}$, $P_{5,2}$, $P_{6,2}$, and $P_{6,3}$; a "South-West light curve" from pixels $P_{6,3}$, $P_{6,4}$, $P_{5,4}$, $P_{5,5}$, and $P_{4,5}$; and a "South-East light curve" from pixels $P_{4,5}$, $P_{3,5}$, $P_{3,4}$, $P_{2,4}$, and $P_{2,3}$. The optimal aperture light curve for these Q5 data was obtained with pixels $P_{4,2}$, $P_{3,3}$, $P_{4,3}$, $P_{5,3}$, and $P_{4,4}$.

The Lomb Scargle periodograms associated with these time series are illustrated in Fig. B.3. The central panel shows the signal centered on KIC 05807616 (optimal aperture) where the two low-amplitude low-frequencies that we associate with planet candidates are visible. Clearly, some of the light coming from KIC 05807616 leaks into the surrounding pixels used to build the light curve in the various quadrants, as the pulsations remain detectable, although more diluted in the background. The important finding, however, is that there is no trace of the low frequency modulations around KIC 05807616. If these were due to the highly diluted contribution of a fainter contaminating star, they would emerge at higher amplitudes in one of the quadrants.

Another more interesting check can be performed by looking at each pixel separately. The cost is a reduced signal-to-noise ratio and therefore a more difficult detection of the very low amplitude modulations. The Lomb Scargle periodograms associated with each pixel within the mask are represented in Fig. B.5. In pixel $P_{4,3}$ receiving most of the flux from KIC 05807616, the strongest among the two low-frequency modulations (F_1) is seen while the other modulation (F_2) remains probably hidden in the noise. In the four adjacent pixels also used to build the optimal aperture photometry ($P_{4,2}$, $P_{4,4}$, $P_{3,3}$, and $P_{5,3}$), these modulations are no longer visible, as the noise is higher. Moreover, in all other pixels we find no indication of modulations at these low frequencies. Therefore the only region where F_1 is seen is in the 3.98"-size pixel closest to the photometric center of KIC 05807616 on the CCD.

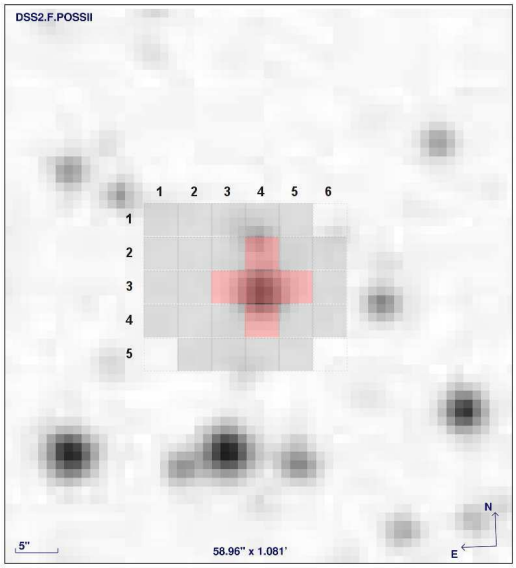

Figure B.2. The field centered on KIC 05807616 with the pixel array mask used during the Q5 run. The pixel size is 3.98" and those in red form the optimal aperture used to compute the time series. Note that the background image is from DSS2 and does not represent the actual PSF on the Kepler CCDs.

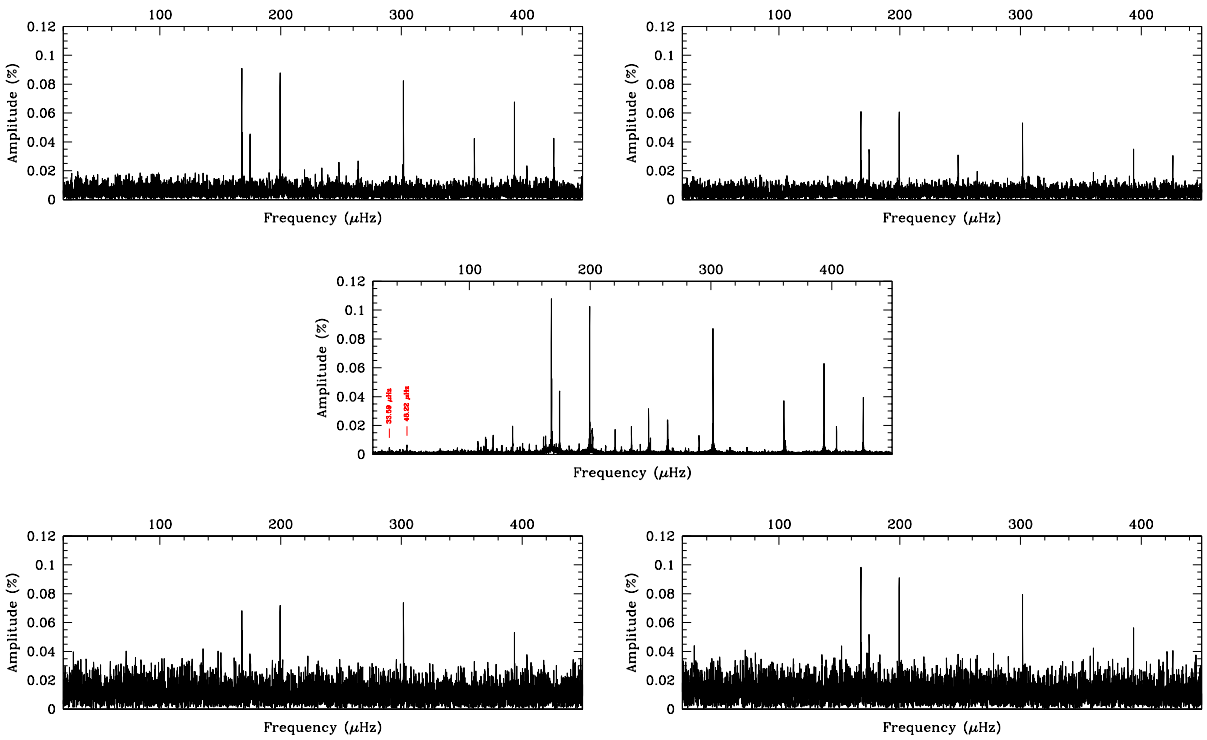

Figure B.3. Lomb-Scargle periodogram of the Q5 light curve using different masks. The central panel corresponds to the optimal aperture mask and other panels show adjacent pixels selected in the North East (upper left panel), North West (upper right panel), South West (lower right panel), and South East (lower left panel) region, respectively. Note that all panels use the same frequency and amplitude scale to ease comparisons. The positions of F_1 and F_2 are indicated by red vertical segments, but only where they are effectively detected (i.e., in the central panel).

Interesting indirect information can be obtained by looking at the amplitudes of the pulsation peaks. Although the amount of light gathered in a given pixel directly affects the noise level in the Lomb Scargle Periodogram, the amplitude of the pulsations measured in each pixel should remain the same unless there is some light dilution (from a contaminating source) affecting the pixels in a differential way. It is striking from Fig. B.5 that the amplitude of the pulsations is the same in pixels $P_{4,3}$, $P_{3,2}$, $P_{3,3}$, $P_{3,4}$, $P_{4,4}$, $P_{5,4}$, and $P_{5,3}$. In contrast, there is a very noticeable decrease of the pulsation mode amplitudes in pixels $P_{4,2}$ (slight decrease), $P_{4,1}$, and $P_{5,2}$. These pixels cover the northern position relative to KIC 05807616 where the close by star visible on Fig. B.1 is indeed located. It is therefore not surprising to observe here a dilution of the pulsation signal (by up to $\sim 50\%$ in pixel $P_{4,1}$). The interesting information, however, is that pixel $P_{4,3}$, where the low frequency modulation F_1 is seen, appears to be essentially unaffected by this dilution. The pulsation modes are at their highest amplitudes, similar to those observed in adjacent, more southerly, pixels. This suggests that the light leakage of the nearby contaminating star is negligible and has no practical impact on this pixel. Therefore, the F_1 modulation that we detect here is almost certainly not associated with this contaminating star. As there is no other sign of non-negligible contamination that could affect this pixel, these light modulations are very likely coming from KIC 05807616 itself. Hence, a false positive due to a contamination of a close by star appears unlikely in the present case.

As an ultimate verification, we assembled the data obtained during Q5, Q6, and Q7 (for a total of 9 months of consecutive monitoring) for the pixel receiving the highest flux. This pixel is the closest to the photometric center of KIC 05807616 on the CCDs which appears essentially unaffected by contamination as discussed above. Merging Q5, Q6, and Q7 runs significantly improves the S/N ratio in the Lomb Scargle periodogram (compared to using only Q5 as above) and compensates for the loss of sensitivity associated with the use of only one pixel for the photometry. The result is shown in Fig. B.4. The two low frequency weak signals that we associate to the presence of planets are clearly detected and emerge at amplitudes identical to those measured in other data sets. It is another confirmation that these peaks must be associated with KIC 05807616 itself.

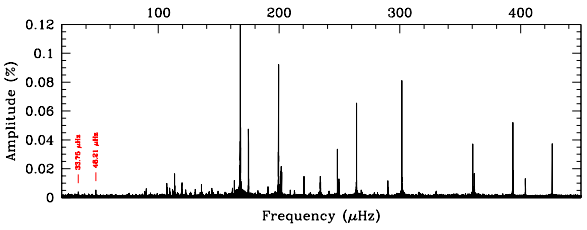

Figure B.4. Lomb-Scargle Periodogram in the pixel closest to the photometric center of KIC 05807616 for the combined Q5, Q6, and Q7 runs.

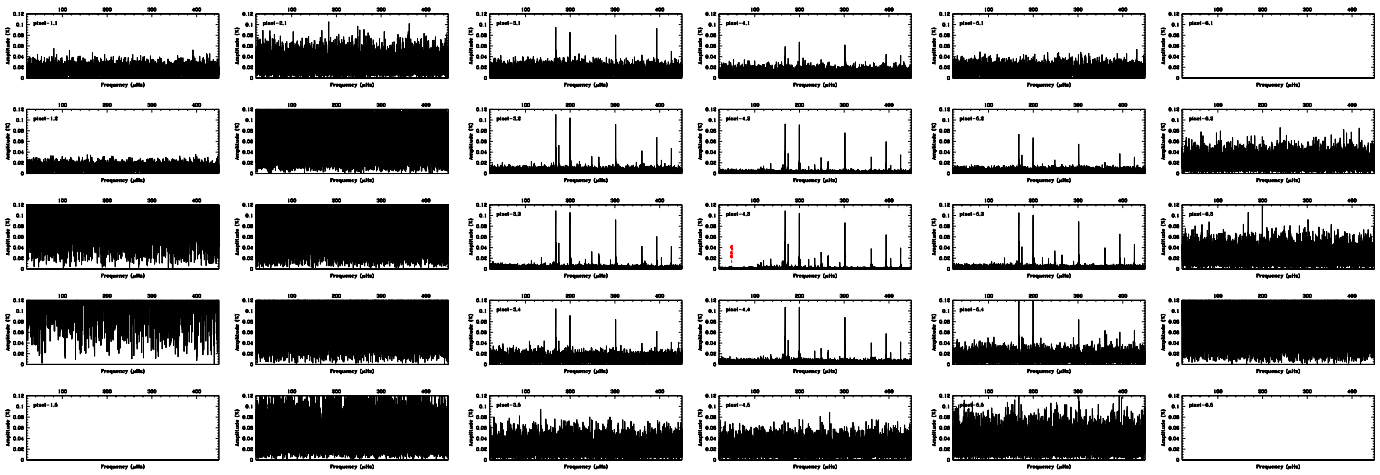

Figure B.5. Lomb-Scargle Periodograms of the Q5 lightcurves obtained at the pixel level. The panel's positions correspond to the pixel array illustrated in Fig. B.2. The same frequency and amplitude scale is used in each panel to ease comparisons. The positions of the orbital modulation candidates are indicated by red vertical segments, but only if they are formally detected. This occurs only for F_1 in the pixel closest to the photometric center of KIC 05807616 (pixel-4,3).

Supplementary Information, Section C: On the origin of the weak signal at low frequencies

In this Section, we discuss various phenomena that could possibly produce the observed modulations in the low frequency range and we provide all the arguments that ultimately lead us to consider an orbital effect due to the presence of small bodies as the most plausible explanation.

C.1. G-mode pulsations?

Since KIC 05807616 is a rich pulsator, we could naturally think of these modulations as just being the tail, at low frequencies, of the g-mode pulsation spectrum. We demonstrate below that this interpretation does not hold, however. We also verified that F_1 and F_2 are not linear frequency combinations of the oscillation peaks having the highest amplitudes.

Figure C.1 shows, in the frequency range of interest, the theoretical g-mode pulsation spectrum corresponding to the seismic model solution found for KIC 05807616 by Van Grootel et al.[15]. In this range, the low frequency end of the observed g-mode band is visible (blue segments), as well as the two low frequencies of interest, F_1 and F_2 (red segments; we ignore F_3 in the following as it is not as firmly established). There is clearly an important gap (in terms of radial orders) between F_1, F_2, and the other frequencies. If F_1 and F_2 were stellar oscillations, they would correspond to very high radial order g-modes, well disconnected from the main group of pulsations observed in this star. As a matter of comparison, the modes of lowest frequencies typically attributed to g-modes in sdB stars have radial orders of $k \sim 65$ at most[15,32]. Here, F_1 would be near $k \sim 83$ (if $\ell = 1$, even more for higher ℓ values) and F_2 would correspond to $k \sim 120$ (if $\ell = 1$). The g-mode spectrum becomes extremely dense at these low frequencies (high radial orders) and having two isolated frequencies emerging among a dense forest of potential modes makes the interpretation of these frequencies as pulsations doubtful.

However, one may argue that a yet unknown pulsation driving mechanism could be at work in KIC 05807616, producing these low-frequency variations. There is indeed one hot subdwarf pulsator, LS IV-14°116, that shows currently unexplained pulsation characteristics[41,42]. This star has periodicities ranging from 1954 to 5084 s corresponding to mid-order g-modes, whereas its effective temperature and surface gravity suggest that it should excite p-modes only, at much shorter periods of 100 to 200 s, that are not observed. Although very different from LS IV-14°116 in its properties, KIC 05807616 may be viewed as another outlier of this kind. However, we demonstrate below that this possibility does not hold, as there is another argument, independent of the driving mechanism involved, against the interpretation of pulsations.

There exists a limit in period (frequency) above (below) which pulsation g-mode waves leak through the stellar atmosphere and are no longer reflected back to the center. This physical limit is called the cutoff period (or frequency) beyond which pulsations modes should not be visible. This cutoff period/frequency can be computed for KIC 05807616 based on the Van Grootel et al. seismic model and solving Eqn. 5 of Hansen et al.[43] (with $\gamma = 0$) derived in the adiabatic approximation. This leads to the cutoff periods (frequencies) $P_c = 16388$ s ($\nu_c = 61.02$ μHz) for $\ell = 1$, and $P_c = 9462$ s ($\nu_c = 105.69$ μHz) for $\ell = 2$. Nonadiabatic effects can possibly affect these values, but the cutoff frequency is primarily a limit depending on the mechanical properties of the modes. These (e.g. the periods and the displacement eigenfunctions) are well known to be marginally affected by the nonadiabatic effects occurring near the surface, contrary to other perturbed quantities very sensitive to thermal exchanges (e.g., the perturbed emergent flux). Therefore, it is unlikely that nonadiabatic effects may affect strongly the estimated cutoff values given above. In particular, such an effect would have to massively increase the cutoff period by 27% (81%) to reach F_1 (F_2).

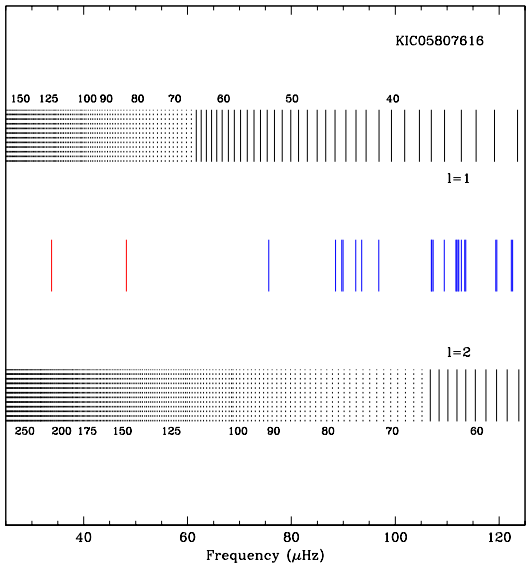

Figure C.1. Theoretical g-mode pulsation spectrum in the 25–125 μHz frequency range computed for the optimal model of KIC 05807616 derived from asteroseismology[15]. The $\ell = 1$ (top) and $\ell = 2$ (bottom) series are compared with the frequencies detected in the *Kepler* data (middle) for this star. The blue segments indicate the frequencies listed in Table A.3 and unambiguously attributed to g-mode pulsations.The red segments represent the two low frequencies of interest, F_1 and F_2. The numbers provided along the computed g-mode series indicate the radial order. Modes shown as dotted segments (instead of plain segments) are below the cutoff frequency.

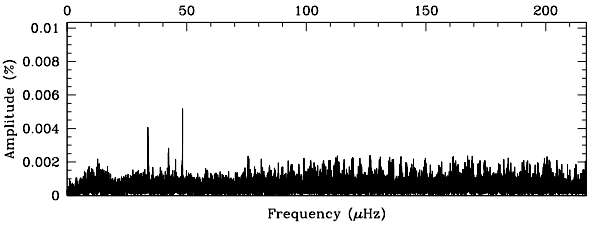

Figure C.2. Lomb-Scargle periodogram in the $0-215$ μHz range after subtracting all frequencies above 60 μHz and 4σ the mean noise level. The low-amplitude peaks of interest (F_1 and F_2), below 50 μHz, are the only significant periodic signals left. A sudden drop of the residual noise at ~ 70 μHz (and below) is clearly visible and likely corresponds to the real pulsation cutoff frequency in KIC 05807616 (estimated to be 61 μHz from adiabatic calculations). F_1 and F_2 are far below this limit, in the 20-70 μHz range, where the residual seems to be dominated by white photon noise contrary to the range above 70 μHz where many oscillation modes below the 4σ detection threshold likely contribute.

Figure C.2 also provides an interesting hint of what should be the real value of the pulsation cutoff frequency in KIC 05807616. After prewhitening all the frequencies above 60 μHz and 4σ the local mean noise level, many extremely low amplitude structures (most likely due to pulsation modes) subsist below the detection threshold. However, near $\sim$ 70 μHz (and below), a sharp drop-off of this remaining "noise" occurs. This sudden change is symptomatic of a cutoff below which pulsation modes are no longer present, and we interpret it as such. We note in this context that the lowest clearly identified frequency associated with a g-mode is 75.64 μHz (see Table A.3). This empirical estimate of the cutoff limit ($\sim$ 70 μHz) is quite consistent with the computed value (61 μHz). The difference possibly comes from several factors such as uncertainties associated with the parameters of the star (and the stellar model used to represent it), and/or simplifications in the computation of the cutoff values (e.g., the use of the adiabatic approximation).

Considering again Fig. C.1 where the modes below the theoretical cutoff frequency are represented as dotted segments, we find that all the frequencies of KIC 05807616 that are interpreted as g-mode pulsations are above at least one of the cutoff thresholds (which occur at a radial order $k \sim 65$), as they should. In this context, we point out that in the star LS IV-14°116 mentioned earlier, the periods detected are also below the cutoff limit (8911 s for $\ell = 1$ and 5144 s for $\ell = 2$ modes, according to the properties of this star[42]) and are consistent with stellar oscillations. In contrast, and more importantly, the two low frequencies F_1 and F_2 in KIC 05807616 stand far below these cutoff frequencies. This excludes the possibility that F_1 and F_2 could be pulsations.

C.2. Stellar rotation and spots?

Modulations can be produced by spots on the surface of an active star. The variations are then caused by the stellar rotation making the spots periodically appear and disappear on the disk facing the observer.

Hot B subdwarfs like KIC 05807616 are very hot stars having stable radiative envelopes and atmospheres on which the presence of spots has, thus far, never been observed or betrayed through brightness modulations. Accordingly, dedicated searches for surface stratifications through Doppler tomography have not yet been attempted with these faint objects. For the He-weak B stars on the main sequence, which share some similarities with sdB stars (in particular the presence of atomic diffusion processes in their atmosphere), Doppler tomography has revealed large spots, in particular of silicon and iron[43]. These spots can be explained by a mechanism that combines chemically fractionned winds from a diffusive atmosphere in the presence of a magnetic field[45]. However, if chemically fractionned winds are conceivable in sdB stars[46], none has ever been detected or confirmed to be magnetic (current upper limits from spectropolarimetry are between 10 to 100 Gauss, typically). Furthermore, for KIC 05807616, there is no evidence of magnetism neither in our optical spectra, nor in the pulsation spectrum observed with *Kepler*. Magnetic splitting differs from rotational splitting and should be recognized if present[35]. The lack of magnetism may indeed not be surprising in a star that have no external convection zone and rotates very slowly (see Section A.3). Therefore, it is unlikely that large spots created by this mechanism could exist on the surface of KIC 05807616.

In any case, whatever the process one could imagine to produce spots on the surface of this star, we stress that the rotation timescale suggested by asteroseismology ($\sim$ 39.23 days; see Section A.3) is much longer than the detected brightness modulations of 5.76 and 8.21 hours. Hence, any link with the rotation of the star is extremely unlikely, and this alone rules out the spot hypothesis.

C.3. Orbiting objects around KIC 05807616?

An alternative interpretation could be the presence of objects orbiting around KIC 05807616 as the timescales are more typical of orbital modulations often seen in compact binary systems including a sdB star as the primary. From Figure 1 (main paper), and from various analysis of the light curve, we find no signs of eclipses at the minimum that could directly betray the presence of a companion. The orbital interpretation is reinforced for F_1 by the fact that the amplitude and phase is constant (within the errors) over a time baseline of $\sim$ 20 months, as one would expect for a stable circular orbit. The case of F_2 may be more questionable due to the complex signature observed in the Lomb-Scargle periodogram. We will nonetheless also interpret F_2 as a possible orbital effect in the following, leaving to Section E some discussions on eventual causes for this fine structure.

Orbital modulations observed in sdB stars are typically due to either a reflection effect when the companion is a low mass main sequence star, or an ellipsoidal effect when the companion is a white dwarf star. However, the intriguing feature in the present case is that the signals are extremely weak, although the periods are relatively short. Therefore, the system is rather compact but still produces tiny effects on the light curve (we recall that F_1 is a 52 ppm modulation, while F_2 is $\sim$ 47 ppm). As interesting comparisons, the eclipsing ellipsoidal sdB+WD variable KPD 1946+4340 monitored with *Kepler*[47] has an orbital period of 9.67 hours and the ellipsoidal effect produces a dominant peak at half the orbital frequency reaching an amplitude of 0.147% (1470 ppm) of the mean brightness. The sdB+dM system KIC 02991403 with a reflection effect[48] has an orbital period of 10.63 hours and the modulation reaches 1.755% (17550 ppm). Both systems are less compact than KIC 05807616 but show orbital modulations that are orders of magnitude stronger. Of course, such low amplitude variations could occur if KIC 05807616 were seen nearly exactly from the pole. There are several additional hints that this is probably not the case:

1. The analysis of the pulsations provides indications of the presence of rotationally split mode multiplets. These suggest a rather slow rotation rate for the star and, from the amplitude distribution of the components within the multiplets, an inclination angle that is likely larger than $\sim 20^\circ$ (see Section A.4 for details). This would exclude that the system is seen nearly pole on.

2. The 2MASS colors for KIC 05807616 are quite blue. The $J-H$ color, in particular is -0.237 ± 0.142. While suggestive of a single sdB star, the error on J-H, unfortunately, does not permit to completely rule out the presence of a dM star at the 2σ level. Furthermore, the color $J-K$ is not reliably determined for this star. However, we point out that, from 3 spectra obtained at the MMT in June 2010 whose timing turns out to sample quite well the orbital phases (see Section C.5), there is no significant radial velocity modulations detected (with an error of $\sim$ 1.2 km.s^{-1} on the measured radial velocities). This dynamical constraint clearly rules out the presence of a companion of mass larger than 0.0057 $M_\odot$ (for F_1) if the orbit is seen nearly edge-on. Alternately, the inclination for a typical dM companion of mass 0.12 $M_\odot$

would have to be less than 2.9° to remain undetectable with our current spectroscopic data.

3. If the star has a white dwarf companion producing an ellipsoidal effect (seen nearly pole on), the dominant modulation would correspond to half the orbital period (contrary to a reflection effect where the modulation period would be equal to the orbital period). Considering the typical mass of a white dwarf (0.6 $M_\odot$) and the rather short periods, we would expect a certain level of tidal synchronization between the stars. Looking closely at the pulsation frequencies extracted from the data, there is, however, no sign of rotational splittings (for $\ell = 1$ or $\ell = 2$ g-modes) that could be associated with a stellar rotation frequency of 24.11 μHz (synchronization + ellipsoidal effect). Moreover, the inclination angle of the system would have to be even lower to make the presence of a white dwarf companion (of typical mass 0.6 $M_\odot$) undetectable in our radial velocity measurements.

4. If we admit that F_2 is also associated with an orbital effect, then KIC 05807616 would have to be a triple system. In this context, the idea that it could be a compact sdB+WD+WD system seen by the pole becomes difficult to envision as a plausible explanation.

5. Finally, it is interesting to note that the period ratio between F_2 and F_1 is ~ 1.43. This ratio is close to the 3:2 resonance that is sometimes seen in systems with multiple orbiting bodies. This configuration is known to be gravitationally stable against perturbations. Unless this correspondence is totally fortuitous, it does plead in favor of orbital modulations involving at least two objects.

The interpretation of orbital modulations is therefore supported by several arguments and it clearly stands out as the most consistent explanation.

C.4. Doppler beaming effect?

If orbiting objects are involved as the above argumentation clearly suggests, the observed modulations may be caused by a Doppler beaming effect. This can be checked by evaluating the expected magnitude of this effect with the available spectroscopic constraint that we currently have.

Doppler beaming has recently been observed in the hot B subdwarf star KPD 1946+4340 monitored by *Kepler*[47]. This star is a double eclipse sdB+WD system whose light curve is dominated by an ellipsoidal modulation coupled with a beaming effect. The detailed analysis of the Q1 short cadence data of this star is reported in the Bloemen et al. paper[47]. The amplitude of the Doppler beaming modulation is given by the relation

$$\frac{\delta F}{F} = \langle B \rangle \frac{v_r}{c} \quad , \tag{C.1}$$

where v_r is the radial velocity, c is the speed of light, and $\langle B \rangle$ is the photon weighted *Kepler* bandpass integrated beaming factor[47]. $\langle B \rangle$ depends on the spectral energy distribution of the star and the instrument spectral response. For the sdB star KPD 1946+4340, this factor was calculated using appropriate sdB model atmospheres, leading to the value $\langle B \rangle = 1.30 \pm 0.03$. It was found in excellent agreement with the value independently evaluated from fitting the light curve, $\langle B \rangle = 1.33 \pm 0.02$.

Using the same model atmospheres we obtain for the somewhat cooler star KIC 05807616[15] a slightly larger value for the beaming factor, $\langle B \rangle = 1.422$. Considering our current upper limit on the measured radial velocity ($v_r \lesssim 2.4$ km/s, at 2σ; Section C.5), we find that a hypothetical Doppler beaming effect would, at best, have an amplitude of 1.14×10^{-5} (or 11.4 ppm). This is significantly lower than the amplitudes measured for F_1 and F_2 (and, in fact, it would be below the detection threshold even with the combined Q2+Q5-Q8 data). If we adopt a less conservative position and consider that $v_r \lesssim 1.2$ km/s (at 1σ), we find that the amplitude of the Doppler beaming would be less than 5.7 ppm. Therefore, this hypothesis is inconsistent with the observations.

Table C.1. Radial velocity measurements obtained from three MMT spectra of KIC 05807616. The S/N values are given per pixel and RV values are heliocentric velocities.

UT date / UT start	Exp. (s)	Air mass	S/N	RV (km/s)	σ_{RV} (km/s)
2010-06-11 / 06:19:42	1200	1.33	84.1	−45.02	1.06
2010-06-11 / 08:52:16	1200	1.03	79.0	−43.23	1.19
2010-06-11 / 10:34:29	1200	1.03	87.3	−44.56	1.15

C.5. Dynamical constraints from spectroscopy

As part of a long term project to measure radial velocities in sdB stars, we obtained three spectra of KIC 05807616 on UT 2010, June 11 with the MMT blue spectrograph using the 832/mm grating in second order (see Table C.1). The spectra extend from 4000Å to 4950Å at a resolution of 1.05Å. They were reduced with standard IRAF tasks, in the same manner as all of our previous sdB MMT spectra. Radial velocities (RV) were obtained by cross-correlating the KIC 05807616 spectra against two extremely high S/N supertemplates from our database which turned out to be excellent matches to the spectrum of KIC 05807616. (18 individual spectra with S/N of about 100 per pixel were shifted and combined to create each of the two RV supertemplates.) The cross-correlations were done using IRAF's FXCOR, after setting the Fourier filter parameters to focus the cross-correlation on the cores of the Balmer lines and the narrow helium and metal lines.

The availability of high S/N templates that are nearly identical to the spectrum of KIC 05807616 significantly improved the accuracy of our RV measurements. Using a self-template built from only the three observed spectra resulted in velocity errors that are larger by a factor of ~ 2. The completely homogeneous nature of our MMT subdwarf spectra (same telescope, instrument, and data reduction procedures), including the spectra used to construct the very high S/N RV templates, is largely responsible for the 1–3 km/s velocity accuracy that we typically achieve. In addition, for these particular KIC 05807616 spectra, 2–3″ seeing conditions combined with careful centering on the 1″ slit essentially eliminated any slit-centering errors.

The RV values given in Table C.1 show no significant modulations. The first spectrum was taken 2.54 h before the second spectrum (i.e., an orbital phase variation $\Delta\phi = 0.44$ for F_1), and 1.7 h separates the third spectrum from the second ($\Delta\phi = 0.30$). Hence, these three spectra correctly sample the orbit and a large modulation, if present, should have been detected. Instead, these data provide an interesting upper limit on potential RV modulations. The achieved accuracy leads to a 1σ error on the RV measurements of ~ 1.2 km/s (Table C.1). A more secure estimate (at 2σ) is that the projected radial velocity variations in KIC 05807616 are below ~ 2.4 km/s.

Supplementary Information, Section D: A detailed evaluation of the hypothesis of planets orbiting around KIC 05807616

In this Section, we investigate the plausibility of the hypothesis of orbiting substellar bodies around KIC 05807616 and we explore exhaustively the impact of the various parameters on the properties of these objects.

D.1. Some general considerations

We can estimate the total luminosity of the system in the *Kepler* bandpass as

$$L = L_* + \sum_j L_j(\text{reflected}) + \sum_j L_j(\text{radiated}) \quad , \tag{D.1}$$

where L_* is the luminosity (in the *Kepler* bandpass) of the star. The L_j's correspond to the luminosity contributions of the jth planet, if more than one object is orbiting around the star (here $j = 1, 2$). The flux of energy in the *Kepler* bandpass available at a distance a_j from the star is $F(a_j) = L_*/(4\pi a_j^2)$. If the planet has an albedo α_j, we can write that

$$L_j(\text{reflected}) = \alpha_j F(a_j) S_j^{(b)} = \alpha_j \frac{L_*}{4\pi} \frac{S_j^{(b)}}{a_j^2} \tag{D.2}$$

where $S_j^{(b)}$ corresponds to the illuminated (bright) surface area of the jth planet projected on the observer's plane (perpendicular to the line of sight) that is indeed contributing to the reflected luminosity. Similarly, the rate of energy absorbed by a planet of radius R_j is given by

$$\mathscr{L}_j(\text{absorbed}) = (1-\alpha_j)\pi R_j^2 \mathscr{F}(a_j) = \frac{1}{4}(1-\alpha_j)\mathscr{L}_* \frac{R_j^2}{a_j^2} \, . \tag{D.3}$$

We point out, in this case, that $\mathscr{L}$ and $\mathscr{F}$ denote the absolute bolometric luminosity and flux, and $\mathscr{L}_*$ is the total luminosity of the star (emitted in the full spectral range).

The way this energy and the associated heating is redistributed on the planet's surface can be particularly complicated. Let us consider a simple model where the illuminated (hot) side of the planet is assumed to be heated at a temperature T_j while the dark (cool) side reaches a temperature $T_j(\text{dark})$. We can define a parameter β such that $T_j(\text{dark}) = \beta T_j$ with $\beta \in [0,1]$. β provides a simple measure of heat redistribution on the surface of the planet. If $\beta = 1$, then the temperature is homogeneous on the planet's surface, while $\beta = 0$ corresponds to the extreme case where all the heat is trapped in the illuminated hemisphere. With this formulation, the total energy radiated per second due to the heat accumulated on the object can be written

$$\mathscr{L}_j(\text{radiated}) = 2\pi R_j^2 \sigma (1+\beta^4) T_j^4 \quad . \tag{D.4}$$

In radiative balance, we have $\mathscr{L}_j(\text{radiated}) = \mathscr{L}_j(\text{absorbed})$ allowing us to estimate the temperature on the hot illuminated side and the cool dark side

$$T_j = \left(\frac{1-\alpha_j}{8\pi\sigma} \frac{\mathscr{L}_*}{a_j^2} \frac{1}{1+\beta^4} \right)^{\frac{1}{4}} \text{ and } T_j(\text{dark}) = \beta T_j \quad . \tag{D.5}$$

The total energy radiated by the planet toward the observer in the *Kepler* bandpass can then be written

$$L_j(\text{radiated}) = 4\left[S_j^{(b)} F_R(T_j) + S_j^{(d)} F_R(\beta T_j) \right] \tag{D.6}$$

where we have defined the total radiated flux $F_R(T_j)$ as

$$F_R(T_j) = \int_0^\infty B_\lambda(T_j) \mathscr{T}_\lambda^K d\lambda \quad . \tag{D.7}$$

The quantity $B_\lambda(T_j)$ is the Planck distribution and $\mathscr{T}_\lambda^K$ represents the *Kepler* instrumental transmission curve (see Fig. D.3). $S_j^{(d)}$ is the planet's dark surface area projected on the observer plane. This quantity is linked to $S_j^{(b)}$, the projected bright surface area, by the relation $S_j^{(d)} = \pi R_j^2 - S_j^{(b)}$.

The projected illuminated surface area depends on the orbital phase, ψ_j, and the inclination angle, i, of the stellar system. We can show from spherical geometry calculations[49] that the projected bright surface area of the planet illuminated by the star and visible for the observer is given by

$$S_j^{(b)} = \frac{\pi R_j^2}{2}(1 + \sin i \sin \psi_j) \quad , \tag{D.8}$$

where $\psi_j = 2\pi t/P_j$ is the illumination phase of the planet following the convention : $\psi_j = 0$, last quarter; $\psi_j = \pi/2$, "full planet"; $\psi_j = \pi$, first quarter; and $\psi_j = 3\pi/2$, "new planet". Here, P_j is the orbital period of the jth planet. The projected dark portion is then simply

$$S_j^{(d)} = \pi R_j^2 - S_j^{(b)} = \frac{\pi R_j^2}{2}(1 - \sin i \sin \psi_j) \quad . \tag{D.9}$$

Gathering all parts together, we can develop Equation (D.1) as

$$\begin{aligned} L \;=\; & L_* + \sum_j \left\{ L_* \frac{\alpha_j}{8} \frac{R_j^2}{a_j^2} + 2\pi R_j^2 \left[F_R(T_j) + F_R(\beta T_j) \right] \right\} \\ & + \sum_j \left\{ L_* \frac{\alpha_j}{8} \frac{R_j^2}{a_j^2} + 2\pi R_j^2 \left[F_R(T_j) - F_R(\beta T_j) \right] \right\} \sin i \sin \psi_j \end{aligned} \tag{D.10}$$

and, considering that *Kepler* is doing differential photometry where only the modulations relative to the mean brightness are recorded, we can finally write

$$\frac{\delta L}{L} \simeq \sum_j \frac{\delta L_j}{L_*} \quad \text{with} \tag{D.11}$$

$$\frac{\delta L_j}{L_*} = \left\{ \frac{\alpha_j R_j^2}{8 a_j^2} + 2\pi R_j^2 \frac{F_R(T_j) - F_R(\beta T_j)}{L_*} \right\} \sin i \sin\left(\frac{2\pi}{P_j} t \right) .$$

Each $\delta L_j/L_*$ contains the contribution of the light reflected on the illuminated surface and the contribution from the temperature contrast between the bright hemisphere and the dark hemisphere modulated by the orbital period, P_j. Recalling further that L_* is the star luminosity in the *Kepler* bandpass, i.e.,

$$L_* \simeq 4\pi R_*^2 F_R(T_*) \quad , \tag{D.12}$$

with R_* being the radius of the star and T_* its effective temperature (here we assume that the star radiates as a black body), the observed semi amplitude, A_j, of this modulation is therefore given by

$$A_j = R_j^2 \sin i \left(\frac{\alpha_j}{8 a_j^2} + \frac{1}{2R_*^2} \frac{F_R(T_j) - F_R(\beta T_j)}{F_R(T_*)} \right) \tag{D.13}$$

allowing us to estimate the radius of the planet candidates

$$R_j = \left(\frac{A_j}{\sin i}\right)^{\frac{1}{2}} \left(\frac{\alpha_j}{8a_j^2} + \frac{1}{2R_*^2}\frac{F_R(T_j) - F_R(\beta T_j)}{F_R(T_*)}\right)^{-\frac{1}{2}} \quad . \quad \text{(D.14)}$$

The last quantity that needs to be estimated is the separation, a_j, of the orbiting planets with their parent star. Assuming that the orbiting bodies have masses, m_j, much lower than the mass of the sdB star, M_*, Kepler's third law provides the needed relationship with the measured orbital period,

$$a_j = \left(\frac{GM_*}{4\pi^2}\right)^{\frac{1}{3}} P_j^{\frac{2}{3}} \quad . \quad \text{(D.15)}$$

Having the radius, we can further assume a mean density, ρ_j, for the planet candidates. This allows us to evaluate their masses

$$m_j = \frac{4\pi}{3}R_j^3\rho_j = \left[\frac{4\pi}{3}R_j^3(i=90^\circ)\right]\rho_j(\sin i)^{-\frac{3}{2}} \quad \text{(D.16)}$$

and the expected radial velocity, assuming circular orbits

$$v_j = \frac{2\pi a_j m_j}{P_j M_*}\sin i = \left[\frac{8\pi^2 a_j R_j^3(i=90^\circ)}{3P_j M_*}\right]\rho_j(\sin i)^{-\frac{1}{2}} \quad . \quad \text{(D.17)}$$

Note that the expected radial velocity increases when the inclination angle decreases because the corresponding increase in radius and mass dominates over the radial velocity geometric projection factor.

These equations provide all the elements needed to evaluate some of the properties of the orbiting objects.

D.2. Properties of the objects assuming light reflection only

Let us first assume that only reflection of the star light on the illuminated surface of the planets is contributing to the modulation. This would be the case if heat on the planet's surface is efficiently redistributed, such that the temperature on the dark side equals the temperature on the bright side (i.e., $\beta = 1$ in our simplified model). In that situation, Equation (D.14) reduces to

$$R_j = a_j\sqrt{\frac{8}{\alpha_j}\frac{A_j}{\sin i}} \quad . \quad \text{(D.18)}$$

and equation (D.5) becomes

$$T_j = \left(\frac{1-\alpha_j}{16\pi\sigma}\frac{\mathscr{L}_*}{a_j^2}\right)^{\frac{1}{4}} \quad \text{and} \quad T_j(\text{dark}) = T_j \quad . \quad \text{(D.19)}$$

An accurate asteroseismic determination of the parameters of KIC 05807616 give a mass $M_* = 0.496\,M_\odot$, a radius, $R_* = 0.203\,R_\odot$, and an absolute luminosity, $\mathscr{L}_* = 22.9\,L_\odot$[15]. With the parameters provided in Table A.1, we find the values given in Table D.1 for the parameters of the two planet candidates. Note that the amplitude of F_2 is more uncertain due to a complex behavior possibly due to a modulation of this frequency (see Section E).

We also assumed two different values for the albedo, one representative of giant planets like Jupiter ($\alpha_j = 0.52$) and one representative of Mercury (a hot telluric planet without atmosphere) and of the currently known hot giant extra solar planets orbiting close to their central star ($\alpha_j = 0.10$)[17–19]. These values span a rather large range likely covering all possible situations. The value of the albedo affects the estimated radii. A small albedo reduces the amount of reflected light and has to be compensated by a larger radius to produce the observed light modulation. Note, however, that the radius scales as the square root of the albedo, thus the impact on the estimated radii is not very strong unless very different values for the albedo are considered. Moreover, a small albedo means more energy absorbed by the planets and possibly a larger modulation due to thermal reemission (see the next Subsection).

Quite interestingly, in both cases, the estimated radii place these objects right in the range of small gaseous giant planets. If the system is seen nearly equator on (but not exactly, as we do not see transits in the light curve), with an albedo of 0.52 (0.10) the two objects would be comparable in size to Uranus and Neptune (Jupiter), with $R_1 \simeq 0.355\ R_J$ (0.809 R_J) and $R_2 \simeq 0.428\ R_J$ (0.976 R_J; R_J being the radius of Jupiter, i.e, $R_J = 7.1492 \times 10^9$ cm).

Of course, there is an indetermination due to the unknown inclination of the system. The configuration could be seen nearly pole on and the sizes of the orbiting bodies would then be significantly larger. However, Fig. D.1 shows that the inclination has to be particularly low to make the above estimates of the radii significantly larger than the radius of a planet of Jupiter size. In order to have $R_j > 1.5\,R_{\rm Jup}$, i should be $\lesssim 3.5^\circ$ for the planet candidates (with $\alpha_j = 0.52$; this values is $i \lesssim 20^\circ$ with $\alpha_j = 0.10$). The chance that the system is seen under such a small inclination is low. Furthermore, constraints on the inclination come from asteroseismology based on the amplitude distribution of rotationally split mode multiplets, suggesting that $i \lesssim 20^\circ$ is very unlikely and possibly points toward an inclination $i \sim 65^\circ$ (Section A.4).

Table D.1. Parameters for the two planet candidates assuming $\beta = 1$ (reflection only).

Parameter	Planet candidate #1	Planet candidate #2
P_j (h)	5.7625	8.2293
A_j	5.2×10^{-5}	$^\dagger 4.7 \times 10^{-5}$
a_j	8.9698×10^{10} cm 1.290 $R_\odot$ 0.0060 AU	1.13749×10^{11} cm 1.636 $R_\odot$ 0.0076 AU
Assumed albedo, $\alpha_j = 0.52$		
T_j (K)	6 553	5 819
$R_j\sqrt{\sin i}$	2.5370×10^9 cm 0.355 R_J 3.978 R_E	3.0587×10^9 cm 0.428 R_J 4.796 R_E
$m_j(\sin i)^{\frac{3}{2}}$ (M_E)	2.29 (0.2 g/cm^3) 114.5 (10 g/cm^3)	4.01 (0.2 g/cm^3) 200.7 (10 g/cm^3)
$v_j\sqrt{\sin i}$ (m/s)	3.8 (0.2 g/cm^3) 187.4 (10 g/cm^3)	5.8 (0.2 g/cm^3) 291.5 (10 g/cm^3)
Assumed albedo, $\alpha_j = 0.10$		
T_j (K)	7 668	6 809
$R_j\sqrt{\sin i}$	5.7853×10^9 cm 0.809 R_J 9.071 R_E	6.9750×10^9 cm 0.976 R_J 10.936 R_E
$m_j(\sin i)^{\frac{3}{2}}$ (M_E)	27.16 (0.2 g/cm^3) 1357.8 (10 g/cm^3)	47.59 (0.2 g/cm^3) 2379.4 (10 g/cm^3)
$v_j\sqrt{\sin i}$ (m/s)	44.4 (0.2 g/cm^3) 2221.5 (10 g/cm^3)	69.1 (0.2 g/cm^3) 3457.1 (10 g/cm^3)

† This amplitude value is more uncertain.

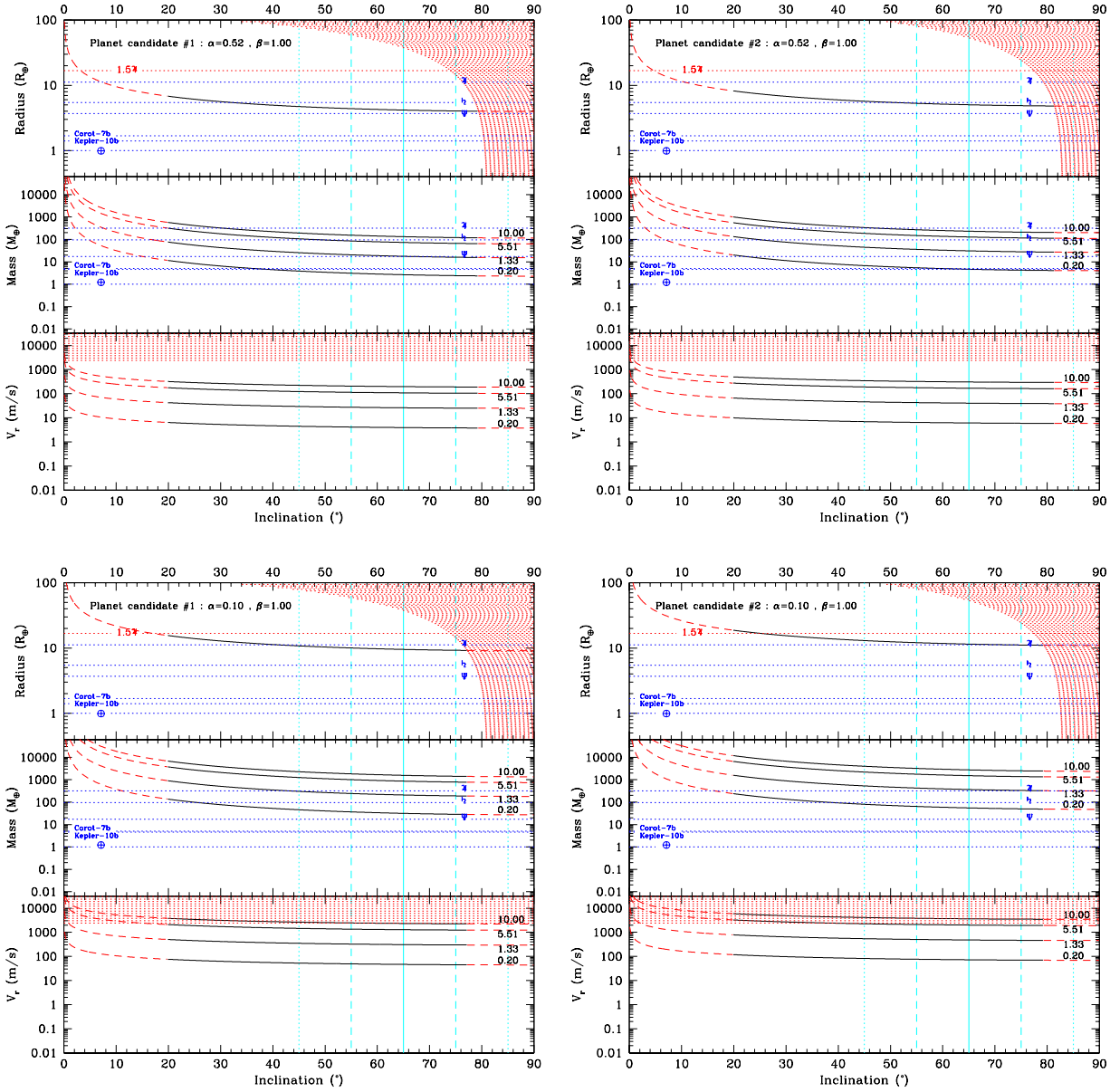

Figure D.1. Estimated radii (in Earth radius), masses (in Earth mass) and radial velocities (in m/s) for the planet candidates as functions of the inclination angle, i, assuming only a reflection effect on the planet illuminated surface. We use two values for the albedo, $\alpha_j = 0.52$ (upper panels) and $\alpha_j = 0.10$ (lower panels). The red filled regions (and dashed portions of the various curves) shows excluded domains due to the absence of eclipses (at large inclinations), due to our current upper limit on the radial velocity modulations (2.4 km/s at 2σ; Section C.5), and due to asteroseismic considerations suggesting that an inclination angle lower than $\sim 20^\circ$ is highly unlikely (Section A.4). The light-blue vertical lines show the suspected angle (65°, plain line) with indications of the 1σ (dashed lines) and 2σ (dotted lines) ranges. The radii and masses of Jupiter, Saturn, Uranus, Corot-7b[29], and Kepler-10b[30] are indicated for comparisons (the blue dotted horizontal lines). We also show the $1.5R_J$ limit (the red dotted horizontal line in radius-vs-inclination subpanels). Four different curves are provided for the mass and radial velocity which sample the typical range of density, ρ_j, where exoplanets are usually found. The values $\rho_j = 5.51$ g/cm^3 and $\rho_j = 1.33$ g/cm^3 correspond to the Earth and Jupiter mean density, respectively.

Considering that no evidence for eclipses is found in the light curve, we can at least set an upper limit to the inclination angle. In order to avoid eclipses, we must have

$$\cos i \geq \frac{R_* + R_j}{a_j} \quad , \tag{D.20}$$

thus excluding the high inclination angles corresponding to the red shaded regions in Fig. D.1. The first planet candidate, the one closest to the star, provides the most stringent constraint on the inclination angle to avoid eclipses, leading to $i \lesssim 79.5^\circ$ when assuming $\alpha_j = 0.52$ ($i \lesssim 76^\circ$ if $\alpha_j = 0.10$). This leaves a particu-

Table D.2. Parameters for the two planet candidates assuming $\beta = 0$ (maximum thermal emission contribution).

Parameter	Planet candidate #1	Planet candidate #2
P_j (h)	5.7625	8.2293
A_j	5.2×10^{-5}	$^{\dagger}4.7 \times 10^{-5}$
a_j	8.9698×10^{10} cm 1.290 $R_\odot$ 0.0060 AU	1.13749×10^{11} cm 1.636 $R_\odot$ 0.0076 AU
Assumed albedo, $\alpha_j = 0.52$		
T_j (K)	7 792	6 920
$\frac{F_R(T_j)}{F_R(T_*)}$	5.934×10^{-2}	3.925×10^{-2}
$R_j\sqrt{\sin i}$	5.7567×10^{8} cm 0.081 R_J 0.903 R_E	6.7398×10^{8} cm 0.094 R_J 1.057 R_E
$m_j(\sin i)^{\frac{3}{2}}$ (M_E)	0.027 (0.2 g/cm^3) 1.338 (10 g/cm^3)	0.043 (0.2 g/cm^3) 2.147 (10 g/cm^3)
$v_j\sqrt{\sin i}$ (m/s)	0.04 (0.2 g/cm^3) 2.2 (10 g/cm^3)	0.06 (0.2 g/cm^3) 3.3 (10 g/cm^3)
Assumed albedo, $\alpha_j = 0.10$		
T_j (K)	9 118	8 097
$\frac{F_R(T_j)}{F_R(T_*)}$	9.698×10^{-2}	6.727×10^{-2}
$R_j\sqrt{\sin i}$	4.6087×10^{8} cm 0.064 R_J 0.723 R_E	5.2626×10^{8} cm 0.074 R_J 0.825 R_E
$m_j(\sin i)^{\frac{3}{2}}$ (M_E)	0.014 (0.2 g/cm^3) 0.686 (10 g/cm^3)	0.020 (0.2 g/cm^3) 1.022 (10 g/cm^3)
$v_j\sqrt{\sin i}$ (m/s)	0.02 (0.2 g/cm^3) 1.1 (10 g/cm^3)	0.03 (0.2 g/cm^3) 1.5 (10 g/cm^3)

† This amplitude value is more uncertain.

larly wide and comfortable range of inclination angles where the estimated radii fall clearly in the planetary range, corresponding to Jupiter-like objects.

Because the sdB star is very hot and luminous ($T_{\rm eff} = 27\,730 \pm 270$ K, $\mathscr{L}_* = 22.9 \pm 3.1\ L_\odot$)[15], and the whole system is particularly compact, the temperatures at the surfaces of these planets are estimated to be very high (see Table D.1). They would be, by far, the hottest "hot Jupiters" ever detected. This directly derives from the other characteristics of this system, namely that these planets would be the ones having the shortest orbital periods known and, thus, being the closest to their parent star. These atypical properties compared with those of known hot giant planets orbiting main sequence stars should not be surprising however, considering the nature of the parent star in this case: an evolved, hot, and compact sdB star.

D.3. Properties of the objects with thermal re-emission

In the previous analysis, we ignored the possible contribution coming from the light radiated by the planets. It is possible (even likely) that a significant thermal imbalance exists between the bright heated hemisphere and the dark cooler hemisphere, producing important temperature gradients. This contribution may induce another source of luminosity modulation added to the pure reflection effect on the planet's surface. As Eqn. (D.14) clearly states, this effect will always contribute to reduce the

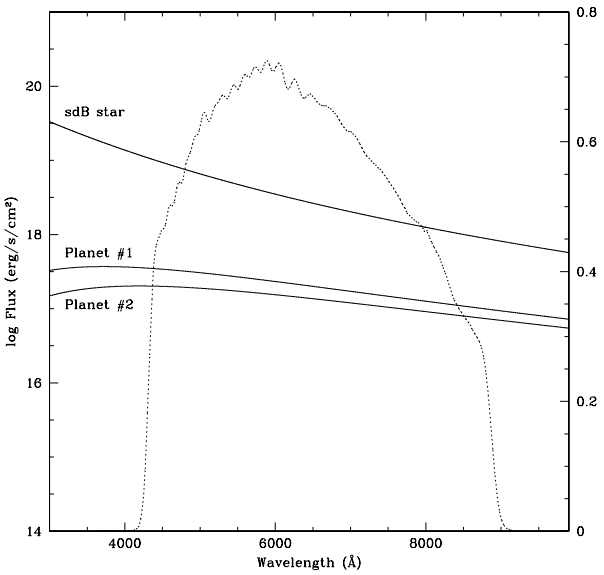

Figure D.3. Estimated blackbody flux emission (on a logarithmic scale) in the *Kepler* wavelength bandpass (the dotted curve shows *Kepler*'s instrument spectral response) for the sdB star and the 2 planet candidates (solid curves), assuming an albedo $\alpha_j = 0.52$.

estimate of a planet's radius compared to the case studied previously. Hence, even if it may be difficult to evaluate precisely this effect, taking it into account will make it even more likely that we indeed see planets, possibly smaller than estimated in Subsection D.2.

We can attempt to estimate quantitatively this contribution by first considering the most extreme case where we set $\beta = 0$ in our simplified model. In this configuration, we consider that only the hemisphere facing the star is heated, while the dark hemisphere receives no heat at all (i.e., we set $T_j(\text{dark}) = 0$ K for simplicity). In this context, Equation (D.14) reduces to

$$R_j = \left(\frac{A_j}{\sin i}\right)^{\frac{1}{2}} \left(\frac{\alpha_j}{8a_j^2} + \frac{1}{2R_*^2}\frac{F_R(T_j)}{F_R(T_*)}\right)^{-\frac{1}{2}} \qquad \text{(D.21)}$$

and Equation (D.5) can be written

$$T_j = \left(\frac{1-\alpha_j}{8\pi\sigma}\frac{\mathscr{L}_*}{a_j^2}\right)^{\frac{1}{4}} \quad \text{and} \quad T_j(\text{dark}) = 0 \quad . \qquad \text{(D.22)}$$

Using this relation, the estimated temperatures on the surface of the illuminated hemispheres of the planets are given in Table D.2. These values can be used to compute the contribution from thermal emission in Equation (D.21). Figure D.3 shows the emitted fluxes in the *Kepler* bandpass assuming blackbody emission for the sdB star (of effective temperature T_*) and the planet candidates (of temperature T_j). We provide the values computed from Equation (D.7) for the ratio $F_R(T_j)/F_R(T_*)$ in Table D.2.

With these numbers, Equation (D.21) provides new estimates for the radii of the orbiting bodies. In the present case, we point out that the contribution from the thermal emission is not a negligible effect. In fact, it largely dominates the star light reflection on the planets' surfaces. This contribution is $\sim 18-20\times$ larger than the reflection when $\alpha_j = 0.52$ is assumed

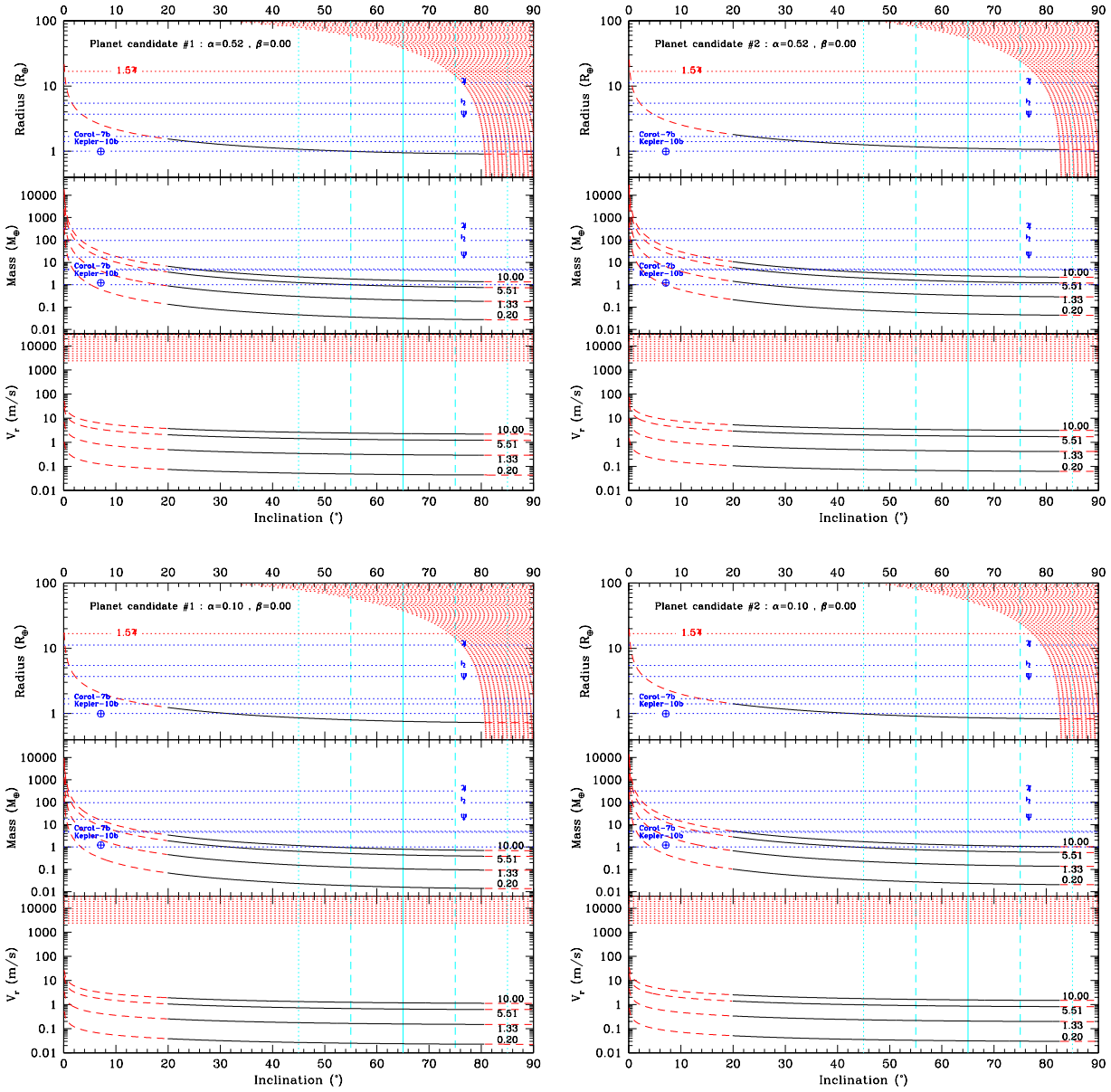

Figure D.2. Same as Fig. D.1 but assuming reflection and thermal re-emission (with $\beta = 0$; i.e. the highest possible contrast between the day side and the night side of the planet candidates).

($\sim 156 - 175\times$ larger, if $\alpha_j = 0.10$). Of course, this corresponds to the largest possible contribution ($\beta = 0$) which decreases if β increases (i.e., if a better energy redistribution on the planet's surface occurs; but see below). In this limiting case, due to the important additional contribution to the modulated flux, the derived radii are significantly smaller than in the hypothesis of pure reflection. Table D.2 summarizes the values obtained in this case, which now indicate that two planets of size comparable to the Earth (or smaller, if small albedoes are assumed) may have been detected. The inferred radii, again, depend on the unknown inclination angle which, however, will significantly affect this conclusion only for very low values of i (Fig. D.2).

A better description of the KIC 05807616 system probably lies in between the two limiting cases discussed previously. The value of β (in the simple model developed) may depend on various factors, such as the nature of the planets (solid, with or without an atmosphere, or gaseous?), whether or not these planets are tidally synchronized such as to always have the same hemisphere facing the star, and other causes. Quite remarkably, however, we find by computing the radii for different values of β based on Equations (D.5) and (D.14) that, very rapidly, the estimated radii become close to the estimation obtained assuming $\beta = 0$. This is illustrated in Table D.3 and Fig. D.4. The reason is that the contrast of light radiated in the *Kepler* bandpass between the hot

Table D.3. Parameters of the two planet candidates as a function of β and assuming an albedo $\alpha_j = 0.10$.

β	T_1 (K)	T_1(dark) (K)	$R_1\sqrt{\sin i}$ ($R_{\rm Earth}$)	T_2 (K)	T_2(dark) (K)	$R_2\sqrt{\sin i}$ ($R_{\rm Earth}$)
0.00	9 118	0	0.723	8 097	0	0.825
0.25	9 110	2 277	0.724	8 089	2 022	0.827
0.50	8 981	4 491	0.764	7 975	3 988	0.867
0.60	8 845	5 307	0.820	7 854	4 713	0.926
0.70	8 641	6 049	0.924	7 673	5 371	1.039
0.80	8 368	6 695	1.121	7 431	5 945	1.257
0.85	8 209	6 978	1.293	7 290	6 197	1.450
0.90	8 038	7 234	1.585	7 138	6 424	1.777
0.95	7 857	7 463	2.226	6 977	6 628	2.500
1.00	7 668	7 668	9.071	6 809	6 809	10.936

and cool hemispheres rapidly becomes large, dominating the effect of light reflection on the planet's surface. Below $\beta \sim 0.8$ (a difference of only 20% in temperature between the two hemispheres), the estimated radii are already comparable to the size of the Earth and suggest planets smaller than the smallest planets discovered around a nondegenerate star so far (Kepler-10b[30] and CoRoT 7b[29]). As a comparison, the estimated mean temperatures on Mercury (i.e., a hot telluric planet without atmosphere) are approximately 450 K on the day side and 90 K on the night side, corresponding to $\beta \sim 0.2$ in our simplified model. Figure D.4 shows that there is indeed a wide range for the parameters where the two extrasolar planet candidates would be the smallest ever discovered.

D.4. Summary

All in all, we estimate that these arguments strongly suggest the presence of two planetary objects of size between the Earth (or slightly smaller) and Jupiter orbiting around KIC 05807616. Moreover, since the planet candidates are very likely tidally synchronized in this case and are showing always the same face to their extremely hot parent star, it is probable that a strong temperature contrast exists between the night side and the day side of the planets (i.e., small values of β). This configuration, according to our estimates, clearly favor planets of small size for all except very small inclination angles (see Fig. D.4). In particular, in the least favorable case where $\alpha = 0.52$, if $i \gtrsim 20°$ ($i \gtrsim 25°$ for planet #2; i.e, still a rather extended range including the angle range suggested by asteroseismology), the planets would be the smallest ever detected orbiting a nondegenerate star other than our Sun.

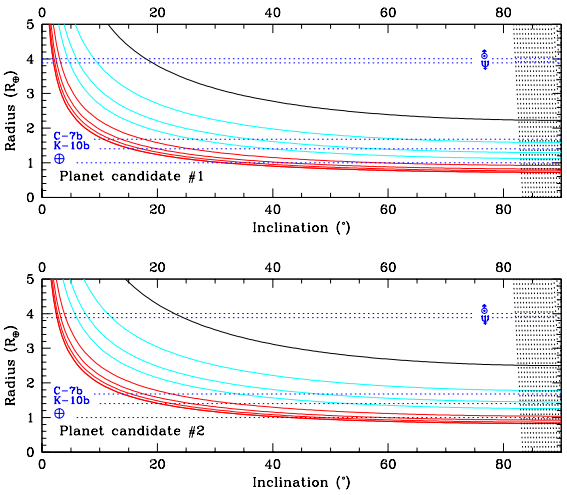

Figure D.4. Estimated radii (expressed in Earth radius) for planet candidates #1 (top) and #2 (bottom) as a function of the inclination angle, i. We assume a geometric albedo $\alpha_j = 0.10$ for the planets and different values for the β-parameter. From top to bottom, the curves correspond to $\beta = 0.95$, 0.90, 0.85, 0.80, 0.70, 0.60, 0.50, 0.25, and 0. The curves in red and light-blue correspond to $\beta < 0.80$ and $0.80 \leq \beta \leq 0.90$, respectively. The radii of Uranus, Neptune, CoRoT-7b (C-7b), Kepler-10b (K-10b), and the Earth are indicated for comparison purposes (the dark-blue dotted horizontal lines). The forbidden eclipse region is also indicated (shaded region at high inclination angles).

Supplementary Information, Section E: On possible causes for the F_2 triplet structure

E.1. Amplitude, frequency, or phase modulations?

The peculiar structure of the F_2 complex is illustrated in Table A.1 and Fig. A.2. This structure forms a symmetric triplet with a frequency separation of $\Delta\nu \sim 0.20$ μHz most visible in the Q5+Q6 subrun. It is is clearly more complex than this, however (see in particular the Q2+Q5-Q8 periodogram). The relative amplitudes of the triplet are difficult to evaluate precisely due to the low S/N of the detection. The observed (and changing) amplitude asymmetries can easily occur from random constructive or destructive interferences with the noise and other structures. Within the uncertainties, one may therefore consider each component to be of comparable amplitude. Interestingly, we also note from Table A.1 that the phases of the side components are equal, although uncertainties on the measured frequencies can significantly change these values. It is noteworthy to mention that oscillation modes split by rotation (see, e.g., Table A.2) do not show specific phase correlations of this kind between their components.

This structure could be indicative of an additional modulation affecting F_2 on a much longer timescale of ~ 57.269 days $(1/2.0 \times 10^{-7})$. The modulation can occur on the amplitude, frequency, or phase, or any combination of these. In Table E.1 and Fig. E.1, we show examples for the three different kind of modulations and their response in Fourier space. The injected signal is noiseless and we used the parameters given in Table A.1 for F_1 and F_2 sampled at 58.8 seconds during the equivalent of 186 day of observation. These synthetic data are therefore comparable to the combined Q5 and Q6 runs (minus the noise).

Considering the properties of the triplet given in Table A.1, the closest configuration arises if the signature is caused by a frequency modulation. An amplitude modulation does not reproduce well the characteristics of the sidelobes. Moreover, a large modulation would be required to produce sidelobes of sufficient amplitude to be detectable in noisy data. The phase modulation also requires a large effect to produce sidelobes of significant size. In contrast, even a small frequency modulation can produces multiplet structures with significant sidelobes. In our ex-

Table E.1. Fourier parameters of a periodic signal with cyclic amplitude, phase, or frequency modulations of 0.20 μHz

Frequency (μHz)	Amplitude (%)	Phase	Comments
Amplitude modulation – $\Delta A/A = 1.0$, $\Delta\psi = \pi$			
33.6249	0.0019	0.1509	
33.8269	0.0037	0.4001	Fig. E.1 (left)
34.0289	0.0019	0.6509	
Phase modulation – $\Delta\mathrm{Ph} = 0.2$, $\Delta\psi = \pi$			
33.6244	0.0014	0.1538	
33.8269	0.0031	0.4001	Fig. E.1 (middle)
34.0284	0.0014	0.1532	
Frequency modulation – $\Delta\nu/\nu = 7.4 \times 10^{-4}$, $\Delta\psi = \pi$			
33.6191	0.0020	0.1915	
33.8230	0.0031	0.4192	Fig. E.1 (right)
34.0200	0.0023	0.2151	
Frequency modulation with noise – $\Delta\nu/\nu = 7.4 \times 10^{-4}$, $\Delta\psi = \pi$			
33.6343	0.0033	0.0019	S/N = 4.7
33.8313	0.0037	0.3631	S/N = 5.3; Fig. E.2
34.0125	0.0026	0.2859	S/N = 3.7

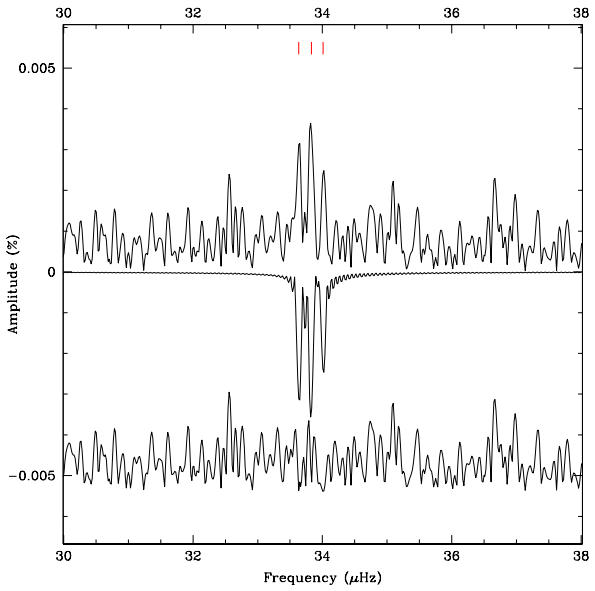

Figure E.2. Lomb-Scargle Periodogram of a synthetic signal modulated in frequency with an added realization of the noise comparable to the *Kepler* data.

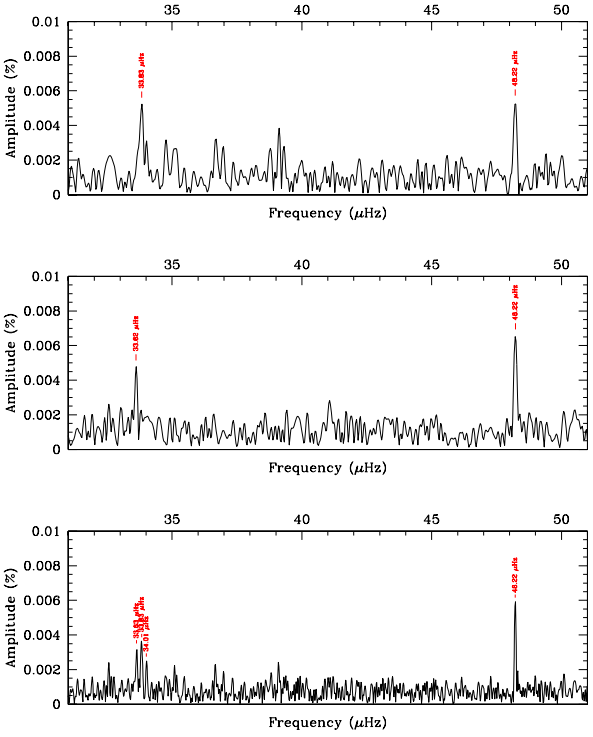

Figure E.3. Lomb-Scargle Periodograms (LSP) of a synthetic signal containing F_1 and F_2. A realization of the noise at a level comparable with the *Kepler* data was added to the synthetic signal. The top (middle) panel shows the LSP of the first (second) half of the synthetic light curve. The bottom panel shows the LSP of the complete synthetic light curve and is comparable to the panel showing the Q5+Q6 data in Fig. A.2.

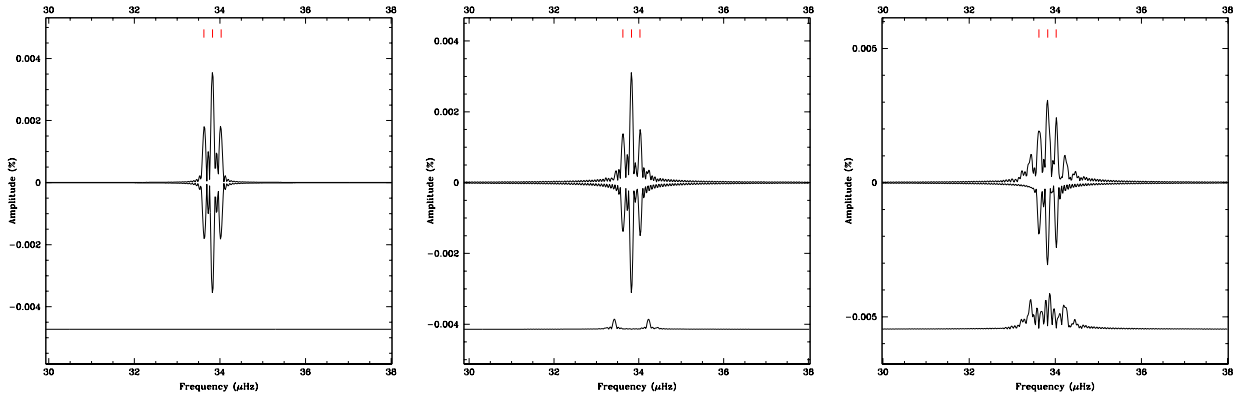

Figure E.1. Lomb-Scargle Periodograms of a noiseless synthetic signal modulated in amplitude (left), phase (middle), and frequency (right).

Table E.2. Frequencies detected above four times the noise level in the complete, 185 day, synthetic data set and in two subsets of 93 day duration.

Id.	Run	Frequency (μHz)	σ_f (μHz)	Period (s)	σ_P (s)	Amplitude (%)	σ_A (%)	Phase	$\sigma_{\rm Ph}$	S/N
F_1	186 days	48.2190	0.0041	20738.693	1.744	0.0060	0.0007	0.562	0.032	8.5
	93 days (part 1)	48.2187	0.0132	20738.841	5.657	0.0054	0.0010	0.567	0.050	5.3
	93 days (part 2)	48.2230	0.0108	20737.004	4.639	0.0065	0.0010	0.513	0.112	6.5
F_2^-		33.6343	0.0072	29731.540	6.393	0.0033	0.0007	0.002	0.059	4.7
F_2	186 days	33.8313	0.0065	29558.468	5.700	0.0037	0.0007	0.363	0.054	5.3
F_2^+		34.0125	0.0094	29400.981	8.107	0.0026	0.0007	0.286	0.076	3.7
	93 days (part 1)	33.8289	0.0132	29560.493	11.529	0.0053	0.0010	0.395	0.051	5.3
	93 days (part 2)	33.6151	0.0149	29748.532	13.192	0.0047	0.0010	0.266	0.155	4.7

ample shown in Fig. E.1 (right hand side), the amplitude of this modulation is only $7.4 \times 10^{-4} F_2 = 0.025$ μHz (or 21.9 seconds in terms of the period). The resulting pattern in the periodogram is a complex structure with dominant sidelobes separated by the modulation frequency (0.20 μHz). Note that, in this case, the central frequency has an underestimated amplitude compared to the one of the injected signal.

In a second step, we produced a synthetic light curve including F_1 and F_2 and we added a white noise at a level comparable with the noise observed in the *Kepler* data. In these synthetic data, the frequency of F_2 was modulated with an amplitude of 0.025 μHz and a modulation frequency of 0.20 μHz (see Table E.1). Note also that F_2 was injected with an intrinsic amplitude of 51 ppm. The Lomb-Scargle periodograms of this noisy synthetic light curve are shown in Fig. E.2 and Fig. E.3. We can see that the complex structures generated by the frequency modulation (right panel of Fig. E.1) are mostly hidden by the noise and only the three dominant components, forming a symmetric triplet, are detectable. Keeping in mind that the noise realization in these synthetic data naturally differs from the realization observed in the real data, Fig. E.3 shows strong similarities with Fig.A.2 (in particular the panel showing the Q5+Q6 subrun).

Interestingly, the Q2+Q5-Q8 run shown in Fig.A.2 (bottom panel) suggests a structure for F_2 which is more complex than a simple triplet. This reinforces the interpretation of a frequency modulation, as the numerous peaks visible in the noiseless data (right hand side of Fig. E.1) should eventually emerge as the noise goes down with more data. However, the full Q2+Q5-Q8 data are clearly not sufficient to characterize these structures and longer time series (probably several years of *Kepler* data) will be needed to exploit further these features.

The parameters of the peaks detected in this synthetic light curve are given in Table E.2 and are similar to the detected signals given in Table A.1. Note, in particular, the apparent frequency variation of F_2 between the two halves of the synthetic light curve and the fact that the true amplitude (51 ppm) is nearly recovered when taking the average of the amplitudes evaluated for the two 93 day sections, while the amplitude of the central component in the fully resolved synthetic data underestimates it. Finally we note that phase estimates for the F_2 triplet components are significantly altered by the noise (see Table E.1) and cannot provide very useful diagnostics. These differences are likely linked to small variations in the fitted frequencies, due to the noise, and these errors propagate to the phase determination.

E.2. Physical interpretation

A clear physical interpretation for the F_2 complex remains elusive at this stage. If we admit the orbital origin of this variation and assume that this structure is caused by a periodic modulation of the frequency/period (of amplitude ~ 0.025 μHz or ~ 22 s; see previous Subsection) over a much longer timescale of 57.269

days, then one may postulate that this structure reflects the presence of another body perturbing mostly the orbit of the second planet candidate. If the period of this frequency modulation is linked to the orbital period of this hypothetical object, then it would be much more distant from the star. Kepler's third law would place it at a distance of $\sim 49.6\ R_{\odot}$ (0.231 AU), i.e., more than 30 times the distance between the star and the two planet candidates. However, perturbation calculations would need to be carried out to test the plausibility of this interpretation.

References

31. Charpinet, S. *et al.* CoRoT opens a new era in hot B subdwarf asteroseismology. Detection of multiple g-mode oscillations in KPD 0629-0016. *Astron. Astrophys.*, **516**, L6-L11 (2010).

32. Charpinet, S. *et al.* Deep asteroseismic sounding of the compact hot B subdwarf pulsator KIC 02697388 from Kepler time series photometry. *Astron. Astrophys.*, **530**, 3-23 (2011).

33. Charpinet, S., Fontaine, G., & Brassard, P. Seismic evidence for the loss of stellar angular momentum before the white-dwarf stage. *Nature*, **461**, 501-503 (2009).

34. Randall, S.K., Fontaine, G., Brassard, P., & Bergeron, P. The Potential of Multicolor Photometry for Pulsating Subdwarf B Stars. *Astrophys. J. Suppl.*, **161**, 456-479 (2005).

35. Unno, W. *et al.* Nonradial oscillations of stars. (Tokyo University Press, 1989).

36. Gizon, L. & Solanki, S.K. Determining the Inclination of the Rotation Axis of a Sun-like Star. *Astrophys. J.*, **589**, 1009-1019 (2003).

37. Balona, L.A. *et al.* Rotation and oblique pulsation in Kepler observations of the roAp star KIC 10483436. *Mon. Not. R. Astron. Soc.*, **413**, 2651-2657 (2011).

38. Charpinet, S. *et al.* Testing the forward modeling approach in asteroseismology. II. Structure and internal dynamics of the hot B subdwarf component in the close eclipsing binary system PG 1336-018. *Astron. Astrophys.*, **489**, 377-394 (2008).

39. Fabrycky, D.C. & Winn, J.N. Exoplanetary Spin-Orbit Alignment: Results from the Ensemble of Rossiter-McLaughlin Observations. *Astrophys. J.*, **696**, 1230-1240 (2009).

40. Moutou, C. *et al.* Spin-orbit inclinations of the exoplanetary systems HAT-P-8b, HAT-P-9b, HAT-P-16b, and HAT-P-23b. *Astron. Astrophys.*, **533**, 113-123.

41. Ahmad, A. & Jeffery, C.S. Discovery of pulsation in a helium-rich subdwarf B star. *Astron. Astrophys.*, **437**, L51-L54 (2005).

42. Green, E.M. *et al.* The Unusual Variable Hot B Subdwarf LS IV-14Â°116. *Astrophys. J.*, **734**, 59-67 (2011).

43. Hansen, C.J., Winget, D.E., & Kawaler, S.D. Upper and lower bounds of periods in variable white dwarfs. *Astrophys. J.*, **297**, 544-547 (1985).

44. Lehmann, H., Tkachenko, A., Fraga, L., Tsymbal, V., & Mkrtichian, D. E. The helium weak silicon star HR 7224. II. Doppler Imaging analysis. *Astron. Astrophys.*. **471**, 941-949 (2007).

45. Babel, J. Multi-component radiatively driven winds from A and B stars. I. The metallic wind of a main sequence A star. *Astron. Astrophys.*. **301**, 823-839 (1995).

46. Unglaub, K. Multicomponent Winds in Sdb Stars? *Balt. Astron.*. **15**, 147-150 (2006).

47. Bloemen, S. *et al.* Kepler observations of the beaming binary KPD 1946+4340. *Mon. Not. R. Astron. Soc.*, **410**, 1787-1796 (2011).

48. Kawaler, S. D. *et al.*. First Kepler results on compact pulsators - V. Slowly pulsating subdwarf B stars in short-period binaries. *Mon. Not. R. Astron. Soc.*, **409**, 1509-1517 (2011).

49. Smart, W.M. Textbook on Spherical Astronomy. Chap. 7, Eqn. 23 (Cambridge University Press, 1977)